

FABRICATION AND A COMPLETE STRUCTURAL, OPTICAL AND
ELECTRICAL ANALYSIS OF POROUS GERMANIUM
NANOSTRUCTURES EMBEDDED IN A DIELECTRIC MATRIX:
POSSIBILITY OF THIRD GENERATION SOLAR CELL APPLICATIONS

A THESIS SUBMITTED TO
THE GRADUATE SCHOOL OF NATURAL AND APPLIED SCIENCES
OF
MIDDLE EAST TECHNICAL UNIVERSITY

BY

BURCU ALTUNTAŞ

IN PARTIAL FULFILLMENT OF THE REQUIREMENTS
FOR
THE DEGREE OF MASTER OF SCIENCE
IN
PHYSICS

SEPTEMBER 2014

Approval of the Thesis:

**FABRICATION AND A COMPLETE STRUCTURAL, OPTICAL AND
ELECTRICAL ANALYSIS OF POROUS GERMANIUM
NANOSTRUCTURES EMBEDDED IN A DIELECTRIC MATRIX:
POSSIBILITY OF THIRD GENERATION SOLAR CELL
APPLICATIONS**

submitted by **BURCU ALTUNTAŞ** in partial fulfillment of the requirements for
the degree of **Master of Science in Physics Department, Middle East
Technical University** by,

Prof. Dr. Canan Özgen
Dean, Graduate School of **Natural and Applied Sciences**

Prof. Dr. Mehmet T. Zeyrek
Head of Department, **Physics**

Prof. Dr. Raşit Turan
Supervisor, **Physics Dept., METU**

Examining Committee Members:

Prof. Dr. Çiğdem Erçelebi
Physics Dept., METU

Prof. Dr. Raşit Turan
Physics Dept., METU

Prof. Dr. Mehmet Parlak
Physics Dept., METU

Assist. Prof. Dr. Mustafa Kulakçı
Physics Dept., Anadolu University

Assist. Prof. Dr. Mücahit Yılmaz
Metallurgical and Materials Eng. Dept., N. Erbakan University

Date: 05.09.2014

I hereby declare that all information in this document has been obtained and presented in accordance with academic rules and ethical conduct. I also declare that, as required by these rules and conduct, I have fully cited and referenced all material and results that are not original to this work.

Name, Last name : BURCU ALTUNTAŞ

Signature :

ABSTRACT

**FABRICATION AND A COMPLETE STRUCTURAL, OPTICAL AND
ELECTRICAL ANALYSIS OF POROUS GERMANIUM
NANOSTRUCTURES EMBEDDED IN A DIELECTRIC MATRIX:
POSSIBILITY OF THIRD GENERATION SOLAR CELL APPLICATIONS**

Altuntaş, Burcu

M.S., Department of Physics

Supervisor: Prof. Dr. Raşit Turan

September 2014, 71 pages

The primary goal of this thesis is to synthesize porous Ge nanostructures embedded in a dielectric matrix and perform a complete structural, optical and electrical characterization. Ge nanostructures can be a good candidate for use in third-generation solar cells, since they are alternative to Si nanostructures owing to their potentially higher photon conversion efficiencies. So far, most of the research is focused on the use of quantum dot structures in photovoltaic applications; although they provide quantum confinement of excitons, their drawback is the difficulties in electrical connection, which relies on tunneling probability through the dielectric matrix. As an alternative, we propose fabrication of porous Ge nanostructures embedded in a dielectric matrix via magnetron-sputtering technique, which is an interconnected Ge nanocrystal network where the electrical connection does not require any tunneling mechanism. We also suggest a way to preserve the quantum confinement effect by

carefully tailoring the Ge content and engineering the structure of dielectric matrix.

Keywords: Magnetron Sputtering, Germanium, Optical characterization, Crystallization, Raman Spectroscopy

ÖZ

GÖZENEKLİGE NANOYAPILARIN DIELEKTRİK MATRİS İÇERİSİNDE ÜRETİMİ VE YAPISAL, OPTİK VE ELEKTRİKSEL ANALİZİ: OLASI ÜÇÜNCÜ NESİL GÜNEŞ GÖZESİ UYGULAMALARI

Altuntaş, Burcu

Yüksek Lisans, Fizik Bölümü

Tez Yöneticisi: Prof. Dr. Raşit Turan

Eylül 2014, 71 sayfa

Bu tezin temel amacı, gözenekli Ge nanoyapılarında dielektrik matris içinde sentezlenmesi; yapısal, optik ve elektriksel karakterizasyonunun yapılmasıdır. Ge nanoyapıların potansiyel olarak yüksek enerji dönüşüm verimlilikleri sayesinde, Si nanoyapılara alternatif olarak üçüncü nesil güneş gözelerinde kullanılması düşünülebilir. Şimdiye kadar olan araştırmalar çoğunlukla kuantum noktacıkların fotovoltaik uygulamalardaki kullanımına yoğunlaşmıştır. Söz konusu yapılar eksitonlara kuantum sınılandırması sağlamasına rağmen, dielektrik matris içerisinde tünelleme olasılığına dayanan elektriksel bağlantı problemleri içermektedir. Buna alternatif olarak, bu çalışmada buhar depolama yöntemi ile (magnetron saçırma) dielektrik matris içerisine gömülü olarak üretilen gözenekli Ge nanoyapıların kullanımı önerilmektedir. Bu Ge nanokristaller bir ağ içerisinde birbirlerine bağlı oldukları için elektriksel bağlantıları bir tünelleme mekanizması gerektirmez. Ayrıca, dielektrik yapısının ve Ge içeriğinin ayarlanması sayesinde kuantum sıkışmasının korunması önerilmektedir.

Anahtar kelimeler: Miknatslı Saçtırma, Germanyum, Optiksel Özellikler,
Kristallenme, Raman Spektroskopisi

To My Family...

ACKNOWLEDGEMENT

First of all, I would like to thank my supervisor Prof. Dr. Raşit Turan for having provided me the opportunity to work in his research group. I am grateful to the examining committee members Prof. Dr. Çiğdem Erçelebi, Prof. Dr. Mehmet Parlak, Assist. Prof. Dr. Mustafa Kulakcı, Assist. Prof. Dr. Mücahit Yılmaz for their valuable comments.

I would like to thank Serim İlday for her guidance, patience, and help. Also, I want to thank my lab mates; Emine Hande Çiftınar, Serra Altınoluk, Olgu Demirciođlu, Zeynep Demirciođlu, Sâlar Sedani, Mona Zolfaghari Borra, Yusuf Kasap, Yasin Ergunt, Buket Gökbakan and all the members of Center for Solar Energy Research and Application (GÜNAM) for their support.

Friends are valuable. However, some of them are very valuable. I am so lucky to meet with Zeynep Nilüfer Güven. Without her great patience, contribution and endless support, I would not have been able to complete this thesis. Besides, I am also very thankful to Fatih Ballı and Murat Öztürk for their great motivation providing me.

I would like to express my deepest gratitude to my family for their endless love, encouragement and trust. I am so lucky to have them. I could not have completed this thesis without them.

Last, thanks to TUSAŞ Aerospace Industries, Inc. (TAI) for the permission to continue my graduate study. I would like to thank all my office mates for their support and patience throughout my study.

I also would thank the Turkish Ministry of Education and Scientific and Technical Research Council of Turkey (TÜBİTAK) for their financial support to this study.

TABLE OF CONTENTS

ABSTRACT.....	v
ÖZ.....	vii
ACKNOWLEDGEMENTS.....	x
TABLE OF CONTENTS.....	xi
LIST OF TABLES.....	xiii
LIST OF FIGURES.....	xiv
LIST OF ABBREVIATIONS.....	xvi
CHAPTERS	
1 INTRODUCTION	1
1.1 Historical Development of Semiconductor Devices	1
1.2 Semiconducting Materials	3
1.2.1 Elementary Semiconductors	3
1.2.2 Compound Semiconductors.....	3
1.3 Optoelectronics.....	5
1.4 Photovoltaic Devices.....	5
1.4.1 Crystalline Si PV Technology	6
1.4.2 Thin Film Crystalline Solar Cells.....	6
1.4.3 Amorphous-Si Thin Film Photovoltaic Technology.....	7
1.4.4 CIS and CIGS Solar Cells.....	7
1.4.5 CdTe Thin film Solar Cells.....	8
1.4.6 Dye Sensitized Solar Cells (DSSC)	8
1.4.7 Organic Solar Cells	8
1.5 Basic Principles of Solar Cells	9
1.5.1 Crystalline Silicon Solar Cells.....	10
1.5.2 Thin Film Solar Cells.....	12
1.6 Motivation of The Work	12

2	NANOCRYSTAL AND NANOSPONGE STRUCTURES FOR OPTOELECTRONIC DEVICES	15
2.1	Theory of Quantum Confinement	15
2.1.1	Two Dimensional Objects	18
2.1.2	One-Dimensional Objects.....	19
2.1.3	Zero-Dimensional Objects.....	20
2.2	Main Physical Features of Si and Ge Nanocrystals	21
2.3	Third Generation Solar Cells Based On Si Nanocrystal	23
3	EXPERIMENTAL	27
3.1	Production of SiGeO Layers by Magnetron Sputtering.....	27
3.1.1	Sample Cleaning.....	28
3.1.2	Magnetron Sputtering System.....	28
3.1.3	Sputtering Parameters	32
3.1.4	In-situ Annealing During The Deposition.....	32
3.2	Characterization and Measurement Techniques.....	33
3.2.1	Raman Spectroscopy (RS).....	33
3.2.2	Transmission Electron Microscopy (TEM).....	34
3.2.3	X-Ray Photoelectron Spectroscopy (XPS).....	35
3.2.4	Ultraviolet-visible Spectroscopy (UV-VIS)	35
3.2.5	Rutherford Backscattering Spectroscopy (RBS).....	36
3.2.6	Scanning Electron Microscopy (SEM)	37
3.2.7	Current-Voltage Measurements (I-V Measurements)	38
4	RESULTS AND DISCUSSION	41
4.1	Properties of as-deposited and deposited samples.....	41
4.2	Ge crystallization during in-situ annealing.....	49
4.2.1	Transmission Electron Microscopy.....	49
4.2.2	Band Gap Estimation	52
4.2.3	Raman Spectroscopy.....	55
4.3	Variations with Ge content	56
4.4	Electric properties of devices made on Ge nanostructures	59

5	SUMMARY AND CONCLUSION	63
6	REFERENCES.....	67

LIST OF TABLES

TABLES

Table 3-1 <i>Magnetron-sputtered and in-situ process samples data</i>	35
Table 4-1 <i>Optical band gap values</i>	54

LIST OF FIGURES

FIGURES

Fig 1-1 <i>The field of semiconductor nanostructures has emerged as a special topic of solid state physics [2].</i>	2
Fig 1-2 <i>Periodic table of elements. Si and Ge in group IV are the examples of elementary semiconductors. Compound semiconductors contain, for example, elements from groups III and V, or II and VI.</i>	4
Fig 1-3 <i>In thermal equilibrium, a p-n junction with zero-bias voltage applied. Under the junction, plots for the charge density, the electric field, and the voltage are shown [12].</i>	10
Fig 1-4 <i>Seven material layers in a c-Si cell [14].</i>	11
Fig 3-1 <i>Schematic view of Ge nanostructures grown by magnetron sputtering.</i> .	27
Fig 3-2 <i>Scattering processes on target material.</i>	29
Fig 3-3 <i>a), b) Schematic diagram of magnetic field, c) Electrons' path above magnetron.</i>	30
Fig 3-4 <i>The nano-D 100 sputtering system.</i>	31
Fig 3-5 <i>Photograph of the sputtering chamber.</i>	31
Fig 3-6 <i>Scattered light energy distribution.</i>	33
Fig 3-7 <i>Rutherford backscattering schematic.</i>	36
Fig 3-8 <i>Simple I-V measurement schematics.</i>	38
Fig 3-9 <i>Schematic view of a specimen used in I-V measurement.</i>	39
Fig 4-1 <i>RBS results of Ge/SiO_x samples (a) As deposited samples, (b) 400 ° annealed samples (c) 600 ° annealed samples.</i>	42
Fig 4-2 <i>RBS results of Ge/SiO_x samples (a) The applied power of Ge 6W, (b) The applied power of Ge 8W (c) The applied power of Ge 10W.</i>	43
Fig 4-3 <i>RBS elemental results of Ge/SiO_x and Ge/GeO_x samples with the applied power of Ge (a) 6W, (b) 8W and (c) 10W, the substrate temperature VS atomic concentration.</i>	44

Fig 4-4 SEM images of the samples deposited in-situ process in 400 °C with applied power (a) 6W, (b) 8W, and (c) 10W.	45
Fig 4-5 SEM images of the samples deposited in-situ process in 600 °C with applied power (a) 6W, (b) 8W, and (c) 10W.	47
Fig 4-6 EFTEM images of 10W RT deposited Ge/SiO _x thin film a) Thin film image on Si Substrate b) The interface of Si substrate and thin film.	49
Fig 4-7 EFTEM images of 10W at 400 °C deposited Ge/SiO _x thin film a) Thin film image on Si Substrate b) The interface of Si substrate and thin film.	50
Fig 4-8 EFTEM images of 10W at 600 °C deposited Ge/SiO _x thin film a) Thin film image on Si Substrate b) The interface of Si substrate and thin film.	51
Fig 4-9 Ge concentration dependence of absorption coefficients at (a) RT, (b) 400 °C, and (c) 600 °C substrate temperatures.	53
Fig 4-10 Change in optical band gap with respect to the Ge concentration at different substrate temperatures.	54
Fig 4-11 Ge concentration and substrate temperature dependence of Raman spectra (a) RT, (b) 400 °C, and (c) 600 °C.	55
Fig 4-12 XPS spectra of (a) Si:2p, (b) Ge:2p ¹ , and (c) Ge:2p ³ for 10W-RT sample.	57
Fig 4-13 XPS spectra of (a) Si:2p, (b) Ge:2p ¹ , and (c) Ge:2p ³ for 10W-400 °C..	57
Fig 4-14 XPS spectra of (a) Si:2p, (b) Ge:2p ¹ , and (c) Ge:2p ³ for 10W-600 °C sample.	58
Fig 4-15 Measured Current-Voltage values of the samples with applied power of Ge (a) 6W (b) 8W (c) 10W at RT.	59

LIST OF ABBREVIATIONS

ABBREVIATIONS

CB	Conduction Band
VB	Valence Band
LED	Light emitting diode
PVD	Physical Vapor Deposition
CVD	Chemical Vapor Deposition
PV	Photovoltaics
RBS	Rutherford Back Electron Spectroscopy
RS	Raman Spectroscopy
SEM	Scanning Electron Microscopy
EFTEM	Energy Filtered Transmission Electron Microscopy
XPS	X-Ray Photo Electron Spectroscopy
DC	Direct Current
RF	Radio Frequency

CHAPTER 1

INTRODUCTION

1.1 Historical Development of Semiconductor Devices

In today's world, modern electronics is used in various fields. It has changed life on our planet during the past fifty years enormously. It has constituted remarkable developments in the industry. Increasing computing power with year by year, studies on this technology is increased significantly both in the industry and scientific fields. The reason for this increase in computer power is the miniaturization of the electronic components that give a good functionality in the same area of a computer chip. This result comes from the decreasing size of transistors. Nowadays, the smallest transistors which are fabricated in industrial research laboratories have a gate length of 10 nm [1].

This tendency towards miniaturization of devices has also affected semiconductor research at universities and research institutes all over the world. To catch the inspiration as the industry, they have to think in deep nanostructure concept which Fig. 1.1 summarizes what the relation in between solid state physics to semiconductor nanostructures [2].

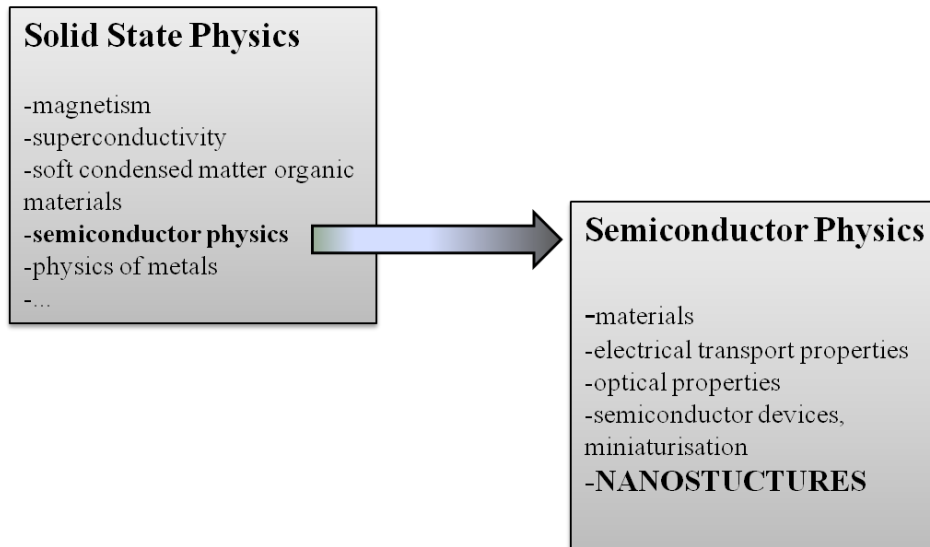


Fig 1-1 *The field of semiconductor nanostructures has emerged as a special topic of solid state physics [2].*

The physics of semiconductors is related to other areas of physics. The relation in between materials science and electronics has mentioned above. In addition to that, modern semiconductor approach is connected with the optics and photovoltaics (PV).

On the other hand, while looking at the energy applications, semiconductors give us the clean energy concept. So what is clean energy? In daily life, in order to obtain the energy for the vital or even routine things, limited energy resources like fossil fuels (coal, natural gas, and oil) are used. This “fossil” fuel reserve is finite. At the current rate of consumption, it is anticipated that only a few hundred years supply is available. In a broad scanning, this increasing rate is going to increase with the developing nations compete for their share of the global economy. In addition to fact that these resources are limited, the use of these stored products of ancient photosynthesis has an increasing price in everyday. Also, as an environmental problem, the carbon-dioxide concentration in the atmosphere increases due to this fossil-fuel consumption.

One way to decrease the consumption of fossil fuels is to use renewable and alternative energy to produce fuels and electricity. Using 1% of Earth's land area, it is possible to supply twice of current energy needs worldwide by converting solar energy at only 10% efficiency [1]. This area could be centrally located, or distributed on rooftops throughout an area where energy is needed.

1.2 Semiconducting Materials

Semiconductor materials are classified as elementary and compound semiconductors:

1.2.1 Elementary Semiconductors

Silicon (Si) and germanium (Ge), phosphorous (P), sulfur (S), selenium (Se), and tellurium (Te), Carbon (C) are elementary semiconductors. Earth's silicon resources are extremely high. Hence, the price of the silicon is cheap in comparison with other semiconductor materials. That is why silicon is very important for the semiconductor industry.

1.2.2 Compound Semiconductors

Compound semiconductors are divided into two groups as II-VI semiconductors and III-V semiconductors as shown in Figure 1.2. Indium arsenide (InAs), gallium arsenide (GaAs), indium antimonide (InSb), gallium antimonide (GaSb), gallium phosphide (GaP), gallium nitride (GaN), aluminum antimonide (AlSb), indium phosphide (InP) and aluminum arsenide (AlAs) belong to groups III and V of periodic table, hence they are named as III-V semiconductors. Furthermore, zinc sulfide (ZnS), zinc selenide (ZnSe) and cadmium telluride (CdTe) belong to II-VI semiconductors.

Group II	Group III	Group IV	Group V	Group VI
	B Boron 5	C Carbon 6	N Nitrogen 7	O Oxygen 8
Mg Magnesium 12	Al Aluminium 13	Si Silicon 14	P Phosphorus 15	S Sulphur 16
Zn Zinc 30	Ga Gallium 31	Ge Germanium 32	As Arsenic 33	Se Selenium 34
Cd Cadmium 48	In Indium 49	Sn Tin 50	Sb Antimony 51	Te Tellurium 52
Hg Mercury 80	Tl Thallium 81			

Fig 1-2 Periodic table of elements. Si and Ge in group IV are the examples of elementary semiconductors. Compound semiconductors contain, for example, elements from groups III and V, or II and VI.

Ge is one of the most popular materials in this semiconductor group due to several reasons. Historically, Ge was firstly used for the production of bipolar transistors. In the mean time, the photo response properties of Ge were discovered [3]. However, Germanium has a lower band gap according to silicon (At 300 K, the band gap of Si is 1.12 eV, and the band gap of Ge is 0.67 eV). Considering the high saturation current of the low band gap of Ge, Si differs from Ge with its larger band gap. Also, Ge crystal growth is possible at low temperatures while Si requires high temperature for crystal growth. Another comparison in between the Ge and Si is the usage for higher speed devices due to electron and hole mobility indicating potential. This comes from the critical Bohr radius which is lower in Ge than Si. Therefore, smaller devices, new insulation schemes and heterojunction growth are now available with Ge. Therefore, as a consequence the use of Ge as components in silicon-based heterojunction circuits is reconsidered.

1.3 Optoelectronics

Photonics and optoelectronics have crucial importance for communication and information technologies. Optoelectronics is the area of research for the integration of device that is controlled by using both optical (light) and electronic properties of materials together. The most important invention of optoelectronics is the fiber optic cables for telecommunication technologies. Optical fiber is a cable which composed of flexible and transparent material made of plastic or silica and used for light (data codes) transmission. Widely used wavelength range for fiber optic technology is near infrared (NIR). However, Si optoelectronic devices are not able to match appropriate responsivity for near infrared and they have self-absorption problem in the waveguide. Si based heterostructures with a lower band gap has solved the mentioned problems. Especially, Ge is the natural choice for those heterostructures by shifting the absorption edge toward the IR. However, Si and silicon-oxide waveguides do not absorb these IR wavelengths. At this point, Ge based heterostructures start to show up.

1.4 Photovoltaic Devices

The physical phenomenon called 'photovoltaic effect' was first observed in 1839 by a French physicist, Edmund Becquerel. In his experiment, silver chloride was connected to platinum electrodes in an acidic solution. When silver chloride was illuminated, voltage and current generated between electrodes. Therefore, the photovoltaic effect can be explained that it is direct conversion of light into electrical energy. As explained, experiments were done in order to measure the voltage difference between electrodes in the conducting solution. However, the photovoltaic effect was then observed with solids (selenium) in 1870s [4]. In the 1880s, selenium photovoltaic cells were produced with 1% - 2% efficiencies. Nevertheless, selenium has several problems. First of all, it can only use the visible spectrum of the sun light resulting in serious conduction problem. One should also consider as a second problem about selenium is the production cost.

However, selenium is a perfect material to use in photometric devices such as light sensitive cells of cameras [5].

Si was firstly named by Scottish scientist Thomas Thomson in 1817. However, the crystalline form of Si was found after 31 years later. After the invention of silicon, solar cell technology has been developed. Due to being first generation PV solar cells, the main technology in the market is still crystalline silicon solar cells. Moreover, when second and third generation photovoltaic devices are considered, they are also up and coming technologies of PV market whereas other kinds of solar cells are still in progress [6].

1.4.1 Crystalline Si PV Technology

One of the most produced PV devices is crystalline Si (c-Si) solar cells in the market according to the total sales. The semiconductor Si is reliable and robust material, and it has high conversion efficiency. From single wafer to solar panel module form, crystalline Si PV cells become common, and that is the reason why the rate of production has showed remarkable performance in recent years. C-Si PV cells can be analyzed into sub groups mainly the crystallinity of the wafer: mono crystal and multi crystal. When mono crystalline wafer based solar cells compared to the multi crystalline ones, they absolutely have higher efficiency and better quality. However, multi crystalline wafers contain different crystalline structures with different crystal orientation. Also, multi crystalline wafers have low production cost, and thus makes them being an alternative to the mono crystalline wafer systems.

C-Si systems have reached very mature level. One important aim in c-Si systems is to decrease the cost. However, when the cost and production advantages are thought, second generation PV technologies, thin film solar cells, are a strong alternative to first generation solar cell technologies.

1.4.2 Thin Film Crystalline Solar Cells

Considering the cost and production advantages, thin film Si solar cells have been an important alternative to other technologies in recent years. It is fabricated on

glass or flexible substrates. In the production process, a single line in the same facility can be traced. This means that all process can be done in an integrated way. In thin film crystalline solar cells, initial investment is quite high, but the cost of operation of these systems is not as high as c-Si ones. However, the main disadvantage of these systems is the low efficiency. Because the quality of the material is low and material thickness is small, there is a low efficiency in these systems.

1.4.3 Amorphous-Si Thin Film Photovoltaic Technology

A-Si thin film can be crystallized by improving the material quality of the a-Si thin film system. Today, in many research laboratories and PV companies are studying on this issue. The main topic of a-Si thin film is to crystalline Si thin films. Because crystallization have a great impact on electrical features of thin film such as resistivity, electron mobility, the fundamental aim is to fabricate high quality thin films in a-Si thin film system. In order to do so, electrical features of the thin film need to be developed such as resistivity, electron mobility.

Recently, there have been reported successful device realizations regarding the a-Si thin films; however, their efficiencies which are produced with the thin film c-Si are still quite low (around 10%) [7]. If the efficiency values increase (like 15%), they can be thought that they are promising for the PV industry. Therefore, research laboratories and PV companies are trying to find new approaches in order to be an alternative a-Si thin film PV technology to c-Si solar cells for the next generation.

1.4.4 CIS and CIGS Solar Cells

The other types of thin film solar cells technology can be exemplified with Copper indium selenide (CIS) and copper indium gallium selenide (CIGS) solar cells are some types of thin film solar cell technology. CIGS has a direct band gap resulting in a high absorption coefficient. Thus, CIGS has the highest efficiency value in thin film solar cell technology. Due to their high efficiency

values, they are considered as promising PV solar cell technology for academy and PV market.

1.4.5 CdTe Thin film Solar Cells

CdTe solar cell technology is the basis of significant advance in thin film technology. They are composed of CdTe absorber and CdS emitter layer in p-n junction structure. High absorption percentages, competitive performance, low production cost and long-term stability make CdTe solar cell popular in PV market. Thus, the production values of CdTe solar cells in the market have reached considerably high values [8].

1.4.6 Dye Sensitized Solar Cells (DSSC)

Dye Sensitized Solar Cell (DSSC) technology was firstly found by Micheal Gratzel and Brian O'Regan in 1991. They found the dye sensitized technology only using the ultraviolet and the blue range of sun light. With the advance in technology, the spectrum is broadened. DSSC is composed of dye molecules having a wide band gap. The main difference between DSSC and a traditional solar cell design is the photosensitive dye separating the photo currents [9]. Moreover, DSSCs have low production cost with the efficiencies up to 11%. Recent advances in fabrication methods enable the semi-transparent or colorful designs of DSSC. However, DSSC technology has some problems as sealing, liquid material usage and life time [8-9].

1.4.7 Organic Solar Cells

Organic solar cells are made of plastic material (i.e. polymer) resulting in relatively low production cost and high market potential. There exist several types of organic solar cell designs according to polymer material used in. However, they have light induced degradation problems resulting in low quantum efficiency and low stability compared to inorganic solar cells. Despite all the problems listed, organic solar cells are promising technology of photovoltaic industry to harvest electricity from sunlight.

1.5 Basic Principles of Solar Cells

The operating principle of PV device is mainly based on the photoelectric effect. In general, the photovoltaic effect means the generation of a potential difference at the junction of two different materials in response to visible or other radiation. The basic processes behind the photovoltaic effect are:

1. *Absorption* of photons, generation of the charge carriers in the materials that form a junction,
2. Subsequent *separation* of the photo-generated charge carriers in the junction
3. *Collection* of the photo-generated charge carriers at the terminals of the junction.

The device mechanism of solar cell is appropriate for these operations. First of all, a solar cell structure consists of an absorber layer, in which the photons of an incident radiation are effectively absorbed. This results in a creation of electron-hole pairs, which are separated from each other by semi-permeable membranes. To build an efficient solar cell, thickness of the absorber layer needs to be smaller than the diffusion lengths of charge carriers for transportation. Membranes can be grouped into two types as n-type and p-type semiconductors. N-type semiconductor membrane blocks holes and pass electrons by having a large conductivity for electrons and small conductivity for holes. At this point, p-n junction principle should be investigated.

In the Fig 1-3, electron and hole concentration are illustrated with blue and red lines, respectively. Gray regions are charge-neutral. Light-red zone is positively charged, and light-blue zone is negatively charged. On the bottom, where the electric field is shown, there is an electrostatic force on electrons and holes. In the direction actuated by electric field, the diffusion tends to move electrons and holes. When p-type and n-type semiconductors are brought together, electron diffusion occurs from n-type to p-type material whereas hole diffusion occurs from p-type to n-type semiconductor. The layer, which electrons and holes pass

through inverse directions, is called depletion region which is also shown in Fig. 1-3. All types of the solar cells have this basic principle to convert solar energy to electrical energy. In the following part, working principles of crystalline Si and thin film solar cells are going to be explained.

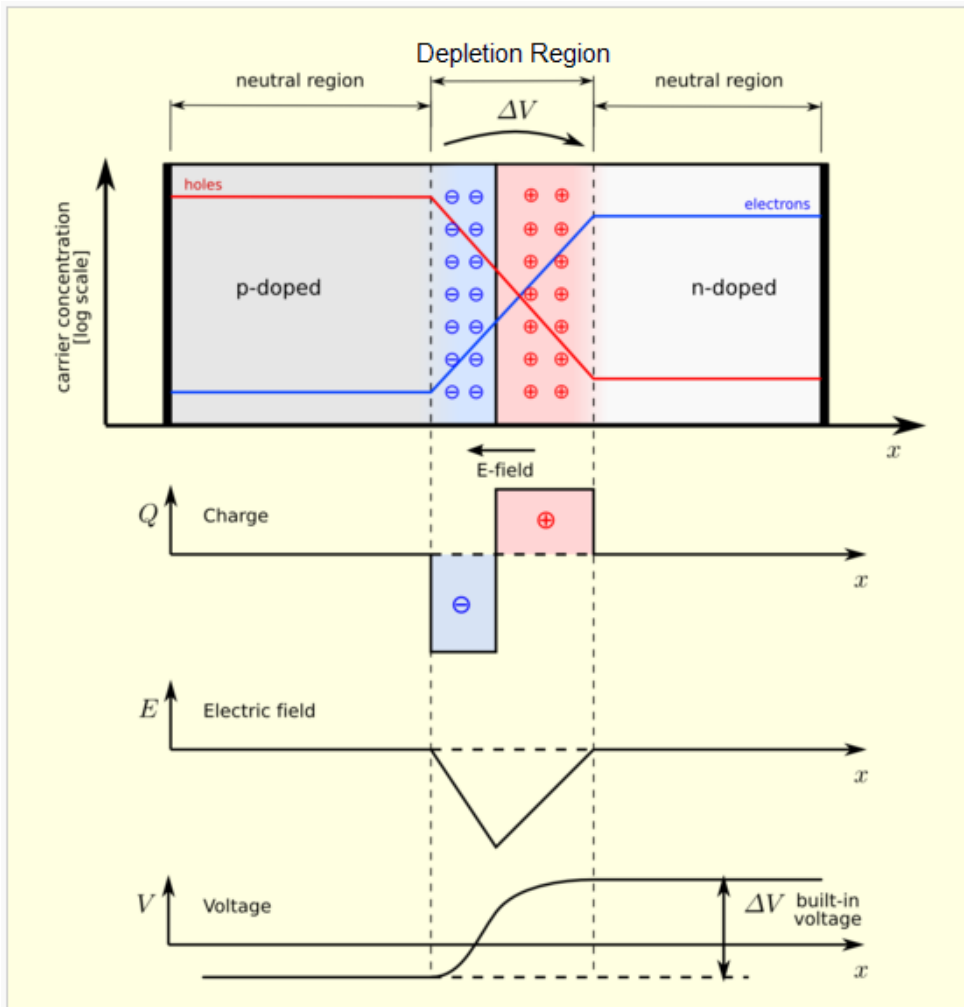


Fig 1-3 In thermal equilibrium, a p-n junction with zero-bias voltage applied. Under the junction, plots for the charge density, the electric field, and the voltage are shown [12].

1.5.1 Crystalline Silicon Solar Cells

Crystalline Si (c-Si) solar cells are the first generation and wafer-based solar cell technology. c-Si solar cells are the most commonly used solar cells as it is

mentioned before. Hence, there is so much reliable information about the features of c-Si in literature. Moreover, c-Si technology has reached the efficiencies between 15% and 25% which is very high compared to other solar cell technologies [13]. A standart c-Si PV module has seven layers; antireflective coating, transparent adhesive, cover glass, front contact, n-type semiconductor, p-type semiconductor and back contact as shown in the Fig. 1-4. Transparent adhesive with protective glass cover over filters the light through layers. N-type semiconductor layer and p-type semiconductor layer aim the electron-hole production to convert the solar energy to electrical energy with the help of electrical circuit shown in the Fig. 1-4.

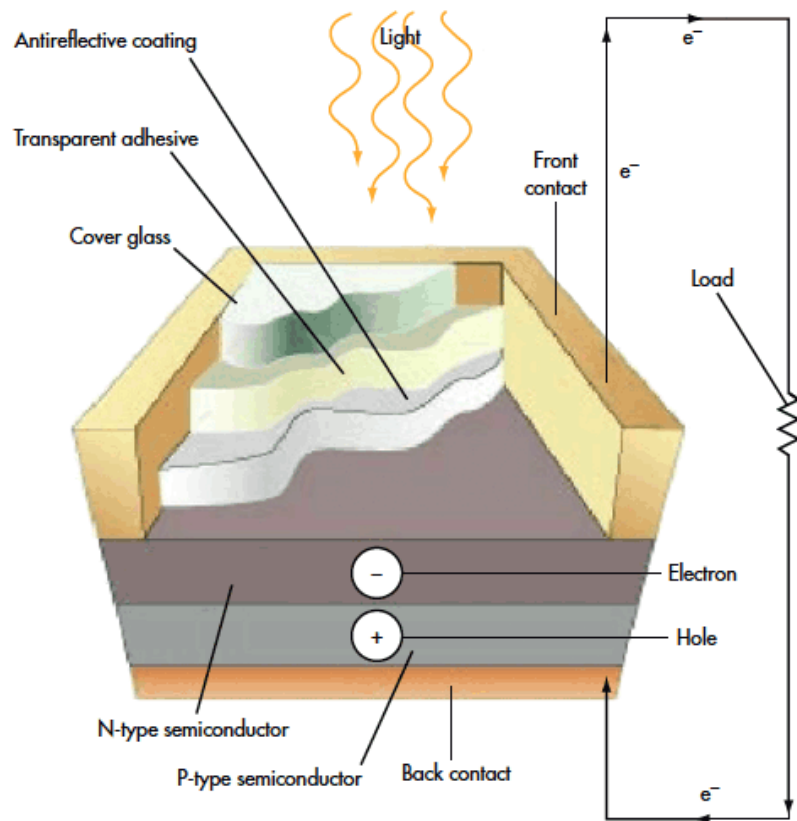


Fig 1-4 Seven material layers in a c-Si cell [14].

1.5.2 Thin Film Solar Cells

Crystalline Si wafers are expensive when the achieved efficiency percentage is considered [14]. However, thin film solar cell production cost is lower than c-Si's. Moreover, thin wafer sheets are not as fragile as c-Si wafers [15].

Thin film solar cells can be basically grouped, according to which material is used, as a-Si, thin film Si, CdTe, dye-sensitized solar cell, copper indium gallium diselenide (CIGS) and other organic materials as it is explained in Section 1.4.

Thin film solar cell structure is more complex than c-Si solar cell structure. They are basically composed of seven layers that are anti-reflective coating, covering transparent conducting coating, opposite polarity junction, substrate, Ohmic contact, p-type and n-type semiconductor layers as shown in Fig. 1-5. The operating principle of thin film solar cells is same as crystalline solar cells.

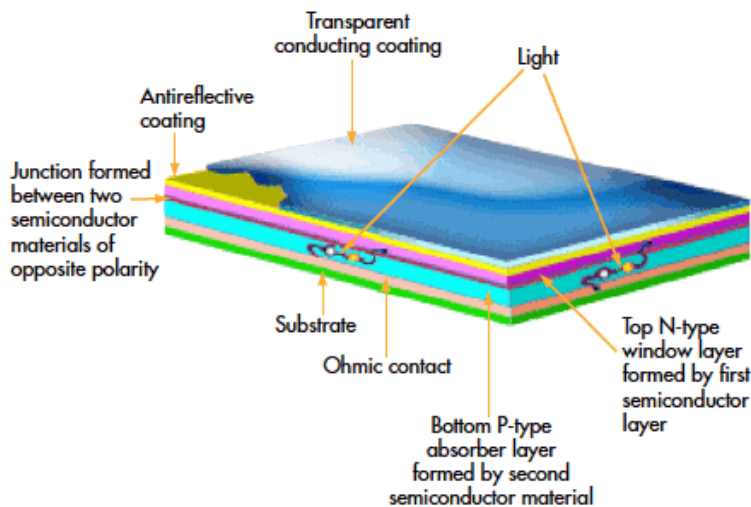


Fig 1-5 A thin film solar cell consists of seven layers [16].

1.6 Motivation of The Work

The optical and electrical properties of Ge ensure large study areas in optics, electronics, and other uses as discussed above. This study is focused on optical

and electrical characterization of Ge nanostructures, and the possibility for the third generation PV applications. To fabricate nc-Ge/SiO₂ thin film, physical vapor deposition technique (PVD) was used. The heater has been working during the deposition, and in-situ process occurred in order to compose a crystalline structure. After the production period, Raman Spectroscopy and optical measurements, Rutherford Backscattering Spectroscopy (RBS), Scanning Electron Microscopy (SEM), X-Ray Photo Electron Spectroscopy (XPS), and Energy Filtered Transmission Electron Microscopy (EFTEM) image analyses and Current-Voltage (I-V) measurements have been fulfilled for characterization of the samples.

- In Chapter 2, nanocrystal and nanosponge structures for optoelectronic devices including solar cells are clarified. Quantum confinement concept is explained briefly.
- In Chapter 3, all the experimental and characterization details are explained.
- In Chapter 4, electronic and optical properties of magnetron-sputtered nc-Ge/SiO₂ thin films are investigated in detail.

CHAPTER 2

NANOCRYSTAL AND NANOSPONGE STRUCTURES FOR OPTOELECTRONIC DEVICES

2.1 Theory of Quantum Confinement

The prefix “nano” means that the dimensions of the particles are in the order of 10^{-9} size. Particles with these sizes are commonly called nanoparticles. If they are in crystalline form, they are defined as nanocrystals. Other names, i.e. quantum dots, also are suggested for these tiny particles which are in the size range of 2-20 nm [17]. With decreasing dimensions, these particles exhibit interesting physical and chemical properties.

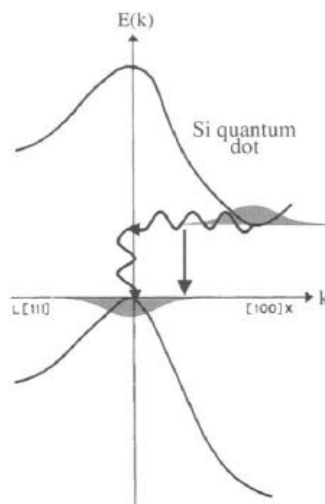


Fig 2-1 Schematic illustration of the effect of spatially confined electrons and holes leading to an enhanced overlap of the carriers' wave functions [18].

Considering the semiconducting materials, they have conduction band (CB, occupied by electrons) and valence band (VB, occupied by holes) as we mentioned in the previous section. By pumping in appropriate amount of energy into the system, electrons (holes) are excited from the VB (CB) to the CB (VB). After creating the e-h pairs, the “quantum confinement effect” is observed because of reducing the size of semiconductor nanocrystals. Due to the particle-wave duality, electrons and holes behave like waves as shown in Fig 2.1. This situation can be broadened to other excitations in the crystal such as excitons and phonons. For the charge carriers and those excitations, the wave description can be correlated a De Broglie wavelength. Quantum confinement of charge carriers, excitons, phonons occurs when the size of volume where these waves are found is comparable to the De Broglie wavelength. Thus, quantum confinement effect is observed when the diameter of the material is lower than the wavelength of excited electron.

In order to understand the theory of quantum confinement, firstly, particle in a box problem should be analyzed. Reducing the size of the materials, discrete energy levels get occurred as a result of quantization effects. This is mainly due to the confinement of the movement electrons. It means that the spacing between the energy levels increases as the length of the box decreases. In the case of semiconductors, it means that the band gap. In Fig. 2.2, energy levels are drawn starting from the bulk value. In the bulk value, the distance between the CB to VB is greater than a nanocrystal's CB to VB. Considering dye sensitized semiconductor concept, quantum confinement effect can be observed clearly regarding the distance in HOMO and LUMO. By the way, HOMO is the valence band edge (VBE) or the highest occupied molecular orbital, and LUMO is the conduction band edge (CBE) or the lowest unoccupied molecular orbital.

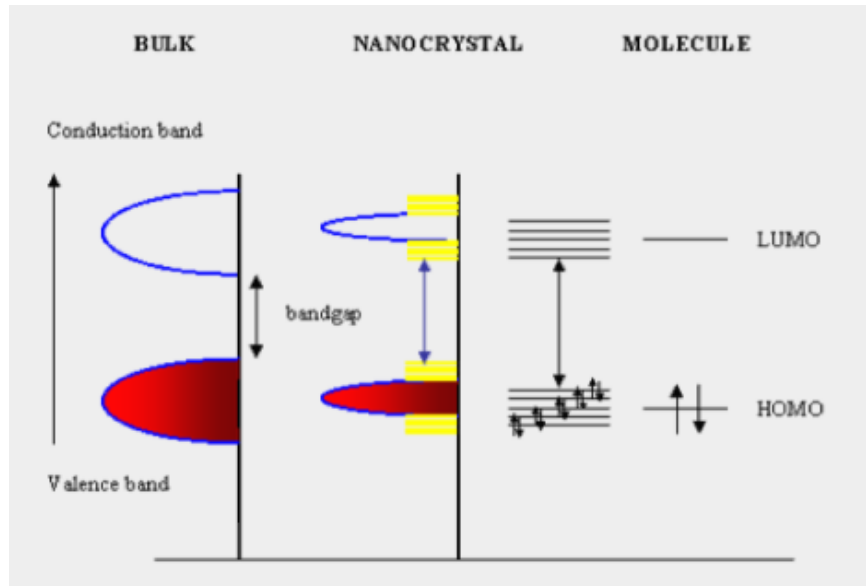


Fig 2-2 In bulk solids the energy levels are closely spaced. Going to the nano-size, due to separation of the energy level, discrete energy levels are observed [19].

One important point is the matrix material. Appearing the nanostructures as free standing structures which are embedded in a matrix material is very interesting at that point. The effect of matrix material to nanostructures is mostly on the electronic levels in the structure. However, our approach for the quantum confinement effect depends on the size of nanostructures. Hence, in case the simple treatments in this thesis, the matrix materials must be taken into account.

Because VB-CB transitions are electronic transitions, they can be observed in the near UV, visible or the near IR region of the electromagnetic spectrum. It is possible to tune the band gap to be at any energy in this range by choosing different semiconductors which have different band gaps [20]. As mentioned in Chapter 1, one application of this discipline is the light emitting diodes (LEDs). Additionally, since nanocrystals absorb all energies higher than their band gap, they can be used as color converters. Another application arises from this point. Sizes of biological molecules are also on the order of a few nanometers. To trace

these biomolecules in medical applications, nanocrystals are being tagged into these proteins [21].

The nanostructures that will be mentioned here can be divided into following categories:

2.1.1 Two Dimensional Objects

Usually, thin films are deposited on a bulk material. Their thicknesses are roughly a few nanometers. Surface and interface effects can dominate their properties. For instance, in the direction perpendicular to the film, the motion of electrons is confined in one direction while they can move in the other two dimensions in the corresponding bulk material. Widely used semiconductor lasers work based on this phenomenon. The band structure of quantum wells in semiconductor laser can be tailored to give the desired emission wavelengths.

In order to understand the physics behind a single quantum well in Fig. 2.3, Schrödinger equation is studied by describing wave functions and energy levels.

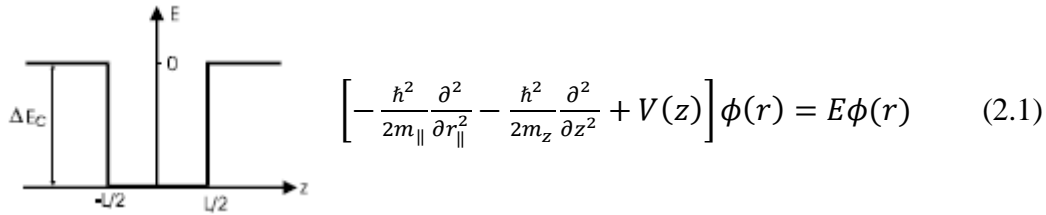


Fig 2-3 A potential well

In space coordinates, this is a second order differential equation. Indices \parallel and z show that the effective masses are in the direction parallel to the interface and in the z - direction.

The solution of the Schrödinger equation becomes within the simple effective-mass approximation and assuming an infinite potential barrier. It can be seen following:

$$E_{gap} = E_n + \frac{\hbar^2 k_{\parallel}^2}{2m_{\parallel}} \quad (2.2)$$

where E_{gap} is the nanocrystal band gap, E_n is the corresponding material band gap, m_1 is the electron-hole reduced mass and k is the wave vector which is equal to $\pm n_x \frac{2\pi}{L}$ where L is the diameter of the nanocrystal. One can deduce from Eqn. 2.2 that the optical gap for a quantum well increases as its size decreases.

2.1.2 One-Dimensional Objects

In that case, the electrons can move in one dimension, and they are confined in the other two directions. This definition is the main concept of the one-dimensional objects. This property can be utilized in large number of applications including light emitting components, sensors, and electronic components.

In Fig. 2.4, it can be seen a structure including a GaAs wire with rectangular cross section in a matrix AlGaAs. Then, one can consider the system with free electron motion in the x - direction and electronic confinement in the y - and z - directions and. Thus, the form of Schrödinger equation as the following:

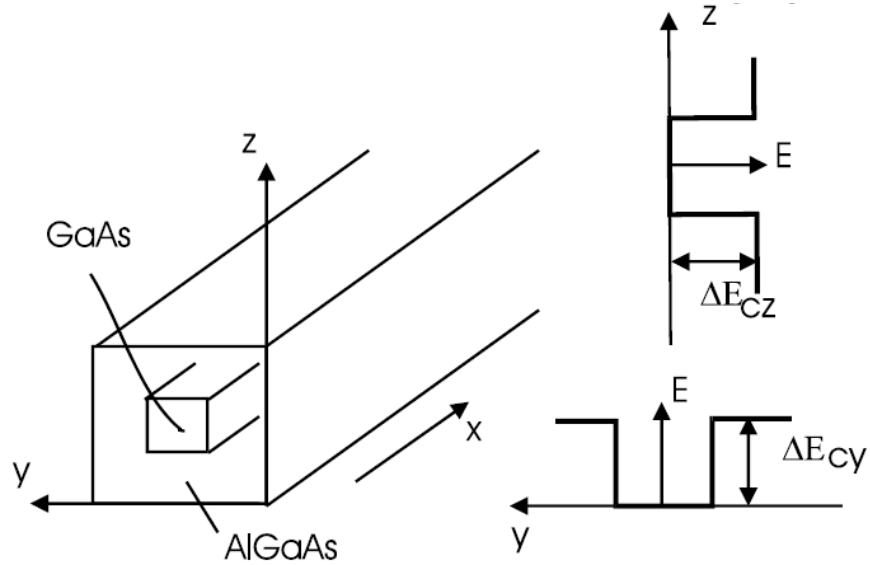


Fig 2-4 The potentials in two directions included a rectangular cross section in a nanowire.

$$\left[\frac{P_x^2 + P_y^2 + P_z^2}{2m} + V(y, z) \right] \Psi(x, y, z) = \Psi(x, y, z)E \quad (2.3)$$

where in the x- and y- directions, the potential can be seen in Fig. 2.4. Free movement is considered as in the x-direction. Assuming the movement independent of the other two coordinates leads to a solution of the form

$$\Psi(x, y, z) = \frac{1}{\sqrt{L_x}} \phi(y, z) e^{ik_x x} \quad (2.4)$$

And the corresponding discrete energies take the form

$$E_{n_y, n_z} = \frac{\pi^2 \hbar^2}{2m} \left(\frac{n_y^2}{L_y^2} + \frac{n_z^2}{L_z^2} \right) \quad (2.5)$$

Assuming that the electrons are free to move along the x-axis and the total energy is

$$E_{gap} = \frac{\pi^2 \hbar^2}{2m} \left(\frac{n_y^2}{L_y^2} + \frac{n_z^2}{L_z^2} \right) + \frac{\hbar^2 k_x^2}{2m} \quad (2.6)$$

2.1.3 Zero-Dimensional Objects

In zero-dimensional systems, electrons are assumed to be confined in all three directions. For instance, nanoparticles, clusters, colloids are composed of several decades to a few thousand atoms as in form of quantum dots, quantum boxes or nanocrystals. These are the examples of the zero-dimensional objects.

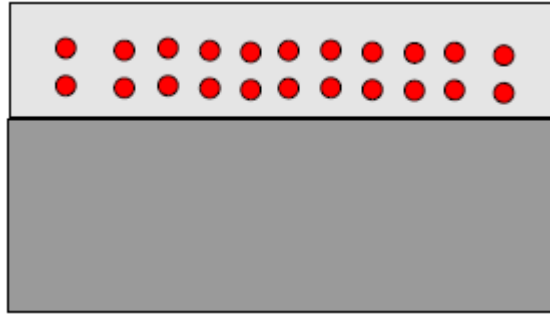


Fig 2-5 *Nanoparticles embedded in a matrix material, i.e. semiconductor nanocrystals in silicon dioxide.*

In that case, one should consider a quantum box whose barriers are infinite and side lengths are L_x , L_y , L_z . Assuming that it is cube with a side length a , the

solution of the Schrödinger equation for electrons and holes (Fig.2.6) takes as in the following form

$$E_n = \frac{\hbar^2}{2m_e} \left(\frac{\pi}{a}\right)^2 n^2, \quad n^2 = \sum_i n_i^2, \quad i=1,2,3,\dots \quad (2.7)$$

$$E_h = \frac{\hbar^2}{2m_h} \left(\frac{\pi}{a}\right)^2 n^2 \quad (2.8)$$

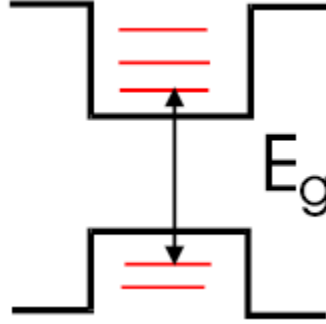


Fig 2-6 CB and VB in the quantum dot.

As a result of quantization effect, the energy gap increases with respect to bulk material. When electrons and holes are considered, in gap energy is described by

$$\Delta E_{gap} = \frac{\hbar^2}{2\mu} \left(\frac{\pi}{a}\right)^2 n^2 \quad (2.9)$$

where $\frac{1}{\mu} = \frac{1}{m_e} + \frac{1}{m_h}$ is reduced mass.

2.2 Main Physical Features of Si and Ge Nanocrystals

In the nanometer scale, reduction in the dimensions of an electronic system modifies the electronic states because of the confinement effect. This leads to change in the properties such as electrical conductivity, optical absorption, or mechanical properties compared to those of the bulk material. The milestone is to monitor single atoms and manage them by using scanning probe microscopy

techniques [19]. After that, in order to fabricate and characterize structures, several methods were improved in nanometer scales.

In research laboratories or institutes, the research for applicable device and system applications of nanostructures is still an ongoing process. “One important issue in fabricating nanometer active areas is the opportunity to fabricate electronic devices operating at frequencies in the 100 GHz up to the terahertz range” says E. Kasper. [22]. From the point of optoelectronics view, T. P. Pearsall states that “The realization of structures on the nanometer scale where quantum effects become more interesting, enables new material properties to be investigated making use of exciton confinement in a three-dimensional (3D) quantum box with distinct energy levels and their associated optical transitions cause distinct emission lines. Furthermore, nanometer-sized active regions in electronic components could allow an increase of integration density in circuits up to 10^{10} elements/cm²” [23].

The development of optical communications and modern optoelectronics has been made possible by the outstanding light-emitting properties of III-V semiconductor compounds that are combined with efficient waveguiding by optical fibers. On the other hand, microelectronics technology relies almost entirely on the use of Si, which conducts a different processing technology making it difficult to integrate optoelectronics (III-V) and microelectronic silicon devices. Conducting these processing technologies requires great effort and financial support. However, bulk Si is known to be poor light emitter due to being an indirect-band-gap semiconductor [18].

On the other case, emission intensity of direct band gap transition with respect to indirect band gap transition increases with the increase in the n-type doping level, injection current density, optical pumping power, temperature and strain [24]. The enhancement of direct band gap transition is due to the increase of electron population in the direct valley by reducing the difference between indirect and

direct band gaps. Thus, both indirect and direct band gap transitions are observed in Ge by electroluminescence and photoluminescence [25].

2.3 Third Generation Solar Cells Based On Si Nanocrystal

The first generation solar cells are based on Si wafers, and they comprise the PV market presently. While this technology has matured, costs have become increasingly dominated by material cost, mostly those of the Si wafer. In the past 20 years, so called thin-film cell technology has been developed. Independent of which semiconductor is used, thin films present for a great reduction in material costs by using less material. Thin films offer other advantages such as producing on large substrates like glass sheet ($\sim 1\text{m}^2$), about 100 times larger than silicon wafer [26]. While considering energy conversion efficiency, second generation technology might expect to catch the same level that of the first generation solar cells.

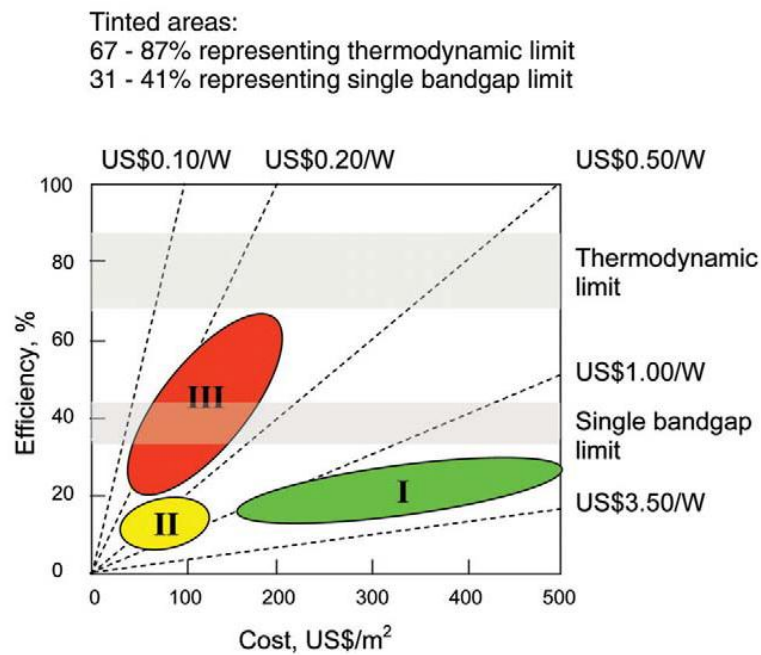


Fig 2-7 Efficiency versus cost projections for 1st, 2nd, and 3rd generation PV technologies [29].

In order to progress further, conversion efficiency needs to be increased gradually. For a standard solar cell, the Carnot limit is 33% on the conversion of sunlight to electricity, while a third generation solar cell upper most limit is 95%. It can be suggested that “The performance of solar cells could be improved 2-3 times if different concepts were used to produce a ‘third generation’ of high performance, low-cost PV product” says M. Green. [27]. Besides, the significant increasing efficiencies, M. Green states that “The aim of third-generation PVs is to reduce costs to well below the \$1/W level of second-generation PVs to \$0.50/W, if even possible to \$0.20/W or better” [28]. Fig. 2.7 shows the efficiency vs. cost projections regarding the three PV generations.

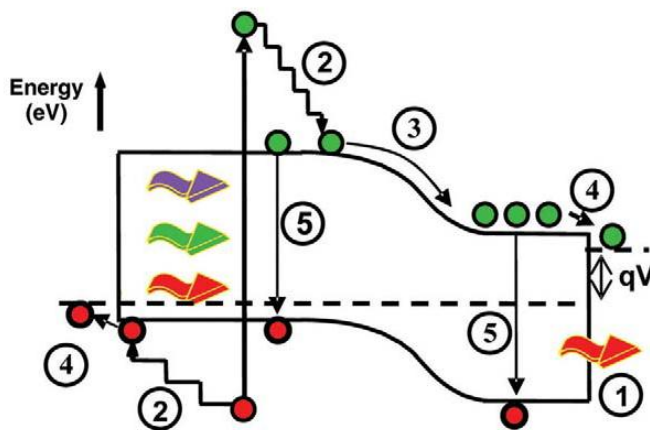


Fig 2-8 Loss processes in a standard solar cell: (1) non-absorption of below band gap photons; (2) lattice thermalization loss; (3) and (4) junction and contact voltage losses; (5) recombination loss [29].

In single band gap cells, loss of power mainly due to the incapability to absorb photons whose energy lower than the band gap (process 1 in Fig. 2.8) and thermalization of photon energies greater than the band gap (process 2 in Fig. 2.8). In solar cell conversion to electricity, these are the two main mechanisms that cause the loss of about half of the incident solar energy. Balancing these

losses with the loss of low-energy photons passing straight through the device alone restricts conversion efficiency of a cell to about 44%. Another important loss process is recombination (process 5 in Fig. 2.8) of the photo excited electron-hole pairs. By using material with high lifetimes for the photo generated carriers, recombination can be kept to a minimum. All undesirable defects in these photo generated carriers must be certainly eliminated. Then, the lifetime is determined by radiative recombination in the cell, the inverse to photo excitation. The relation between light emission and light absorption can be used to achieve fundamental limits on reachable solar cell performance [30]. This manner calls to mind ‘blackbody’ radiation. By relating the light emitted by an ideal cell to that emitted by a black body, Shockley and Queisser showed that the performance of a standard cell was confined to 31.0% efficiency for an optimal cell with a band gap of 1.3 eV. This is lesser than the case of 44% previously mentioned because the output voltage of the cell is less than the band gap potential, with the difference composed of by voltage drops at the contact and junction (Fig. 2.8).

The key loss mechanism recombination which is shown as process 4 in Fig. 2.8 can be possibly eliminated in the case energy of the absorbed photon is higher than cell band gap. This approach leads to the tandem cell concept. In a tandem cell concept, multiple cells are used. Multiple cells include inside with different band gap cells, and these cells can convert a narrow range of photon energies close to each band gap of cells.

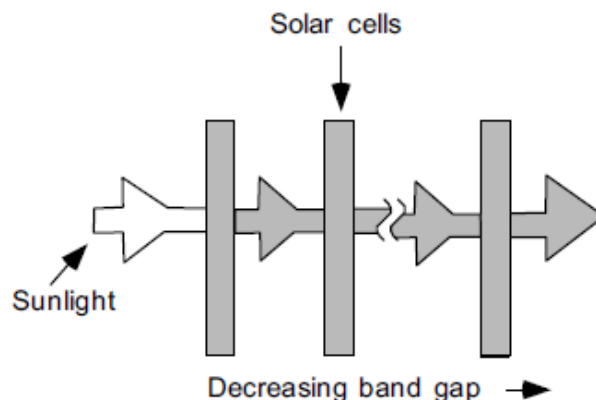


Fig 2-9 Tandem cell approach [31].

Fig. 2.9 shows how the physical mechanism is used in a tandem cell. From highest band gap to lowest band gap, a desired filtering is applied in stacking the cells. Therefore, first absorption starts with the highest band gap, and even the very lowest band gaps can be absorbed. In order to increase the performance of the tandem cell, number of cells can be increased in the stack. Additionally, conversion efficiency for a direct sunlight is stated by Marti as “86.8% for an infinite stack of operated cells” [32].

CHAPTER 3

EXPERIMENTAL

3.1 Production of SiGeO Layers by Magnetron Sputtering

Preparation of samples includes following steps:

- 1 • Si and Quartz Substrate clipping in proper dimensions
- 2 • Sample Cleaning
- 3 • Deposition from Ge and SiO₂ targets
- 4 • Al contacts (for samples used in I-V measurements)
- 5 • Characterization Tests (I-V, Raman Scattering, XPS, RBS, SEM, TEM)

Also,

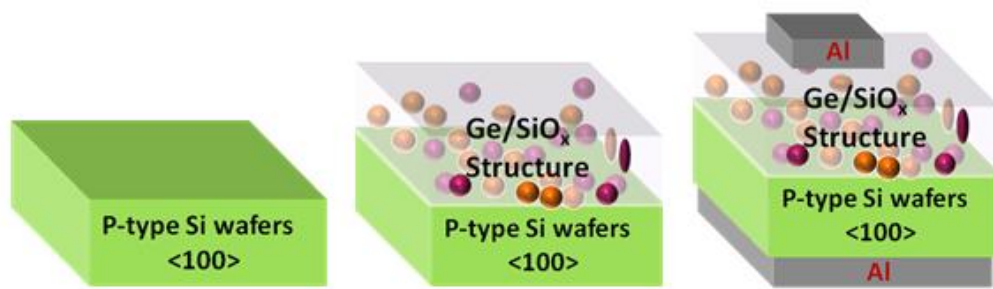


Fig 3-1 Schematic view of Ge nanostructures grown by magnetron sputtering.

Fig 3.1 illustrates schematic view of Ge nanostructures that are used in this study.

3.1.1 Sample Cleaning

P-type Si wafers in [100] crystallographic direction and Quartz substrates were used during the experiments. Firstly, they are cut into appropriate dimensions. Then, they were held in isopropyl alcohol. To clean the oxide layer at the top of substrates, quartz ones were dipped into only 5% of the hydrofluoric acid (HF) solution. Substrates were firstly dipped into piranha solution, and then HF solution. Piranha solution is a mixture of H_2SO_4 and H_2O_2 acids (3:1), and it was used only for cleaning the oxide layer from Si [100] substrates. Both of them were flushed with pure water, and dried with nitrogen gun. End of the cleaning process, all oxide layer were cleaned as expected.

3.1.2 Magnetron Sputtering System

The sputtering process (it is also known as physical vapor deposition) involves a bombardment of germanium and SiO_2 solid targets by energetic ions; i.e. argon ions. In order to deposit the substrate, target materials germanium and SiO_2 were used. Energetic ion particles scatter the atoms and molecules from the target material, and scattered particles turn in the direction of substrate material. This occasion depends on inelastic collisions on the target's surface. When surface atoms gain energy larger than the surface binding energy and momentum out of target's surface, sputtering begins. A schematic view of this process is shown in Fig. 3.2.

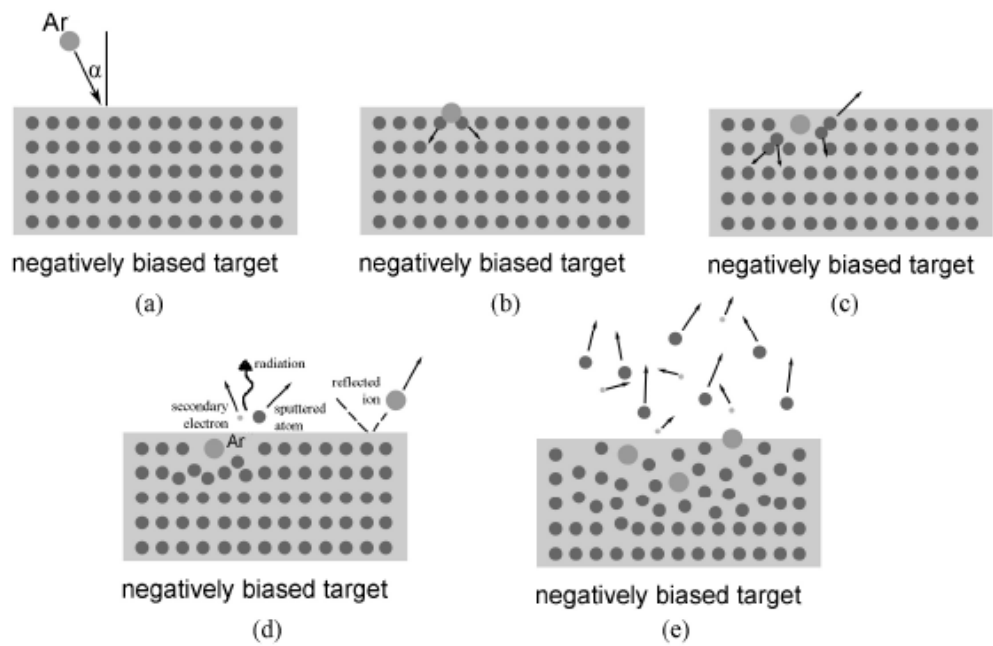


Fig 3-2 *Scattering processes on target material.*

In order to increase the deposition rate, magnetic field is added to the sputtering system. In the magnetron sputtering system, ion density in the plasma is supported and increased by trapping electrons near target surface in the magnetic field. Hence low pressure sputtering (up to 10^{-5} torr) with high deposition rate can be performed. Permanent magnets or electromagnets can be used at different geometries to obtain uniform magnetic fields parallel to the target's surface and perpendicular to electric field so electrons follow circular spiral path as shown in Fig. 3.3 [42].

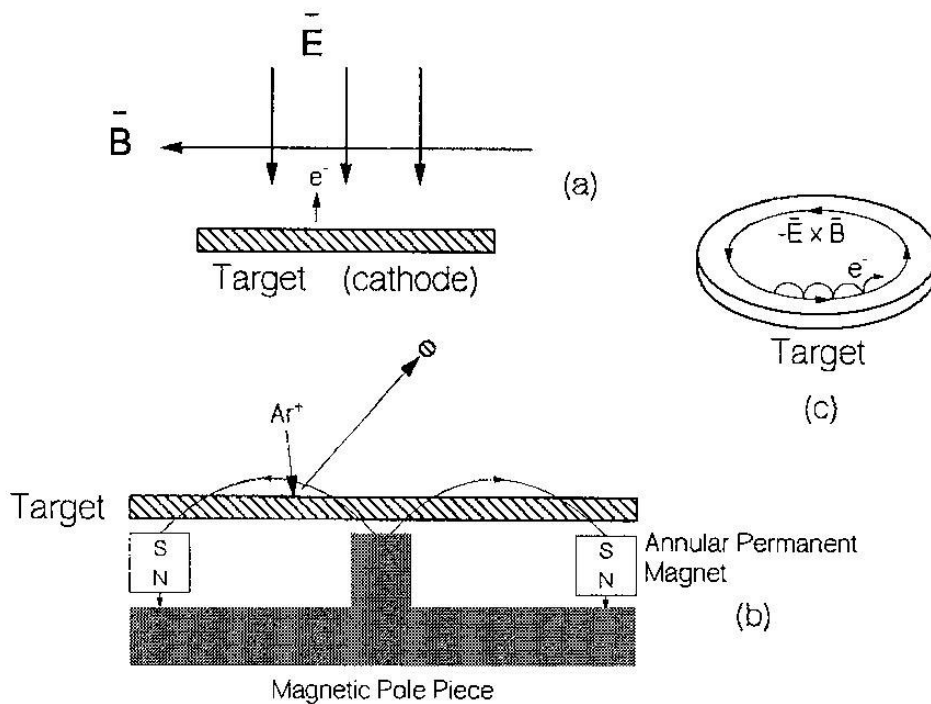


Fig 3-3 a), b) Schematic diagram of magnetic field, c) Electrons' path above magnetron.

In this thesis study, Nano-D 100 has been used which is a multi target, capacitively coupled DC and RF magnetron sputtering system manufactured by Vaksis LTD. (see Fig. 3.4 and 3.5). Complex structures and compounds can be fabricated using three 3-inch circular magnetrons installed as shown in Fig. 3.5. For the experiments that are going to be mentioned here, one of the magnetrons is connected to 600W 13.56MHz RF power supply and other one 500W DC power supply. Last one has not been used for this study. By using Nano-D 100 system, various conductors and insulator can be co-sputtered. In Nano-D 100, there is also a rotating substrate holder in which up to 2-inch substrates can be mounted. As shown in Fig. 3.5, target to substrate distance and angle is adjustable whose angle is 60°. However, once they are adjusted, they have been kept fixed not to cause a change in the experiments. Base pressure up to 10^{-7} Torr can be achieved with installed turbo molecular pump (TMP). For sputtering gas, Argon is used because of being inert. Also, high purity nitrogen gas is installed to the system.

Substrate can be heated before or during deposition by using heater from the back side up to 1000 °C.



Fig 3-4 *The nano-D 100 sputtering system.*

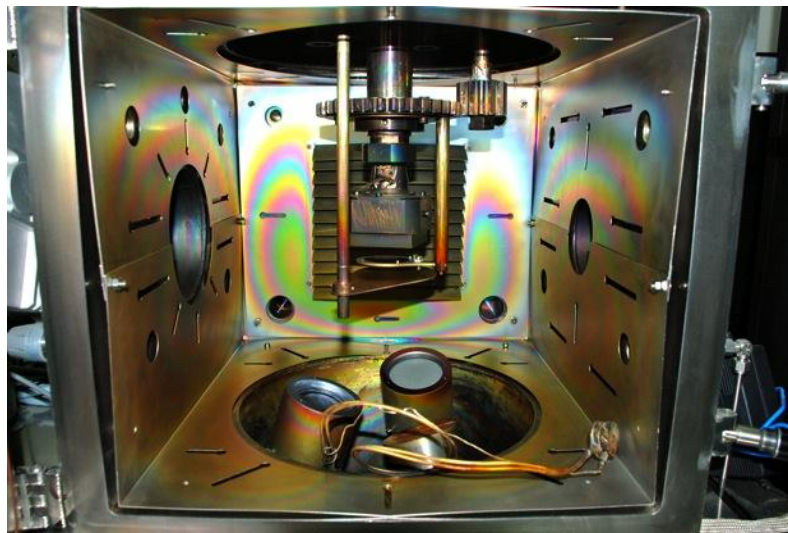


Fig 3-5 *Photograph of the sputtering chamber.*

3.1.3 Sputtering Parameters

Si and Ge nanocrystals embedded in SiO₂ matrix were produced by co-sputtering method. The substrates were p-type Si in (100) crystallographic direction and quartz. Ge and SiO₂ sputtering targets have been simultaneously sputtered in Ar gas with a flow rate 20.0 sccm. The base pressure of the sputtering chamber was around 10⁻⁶ torr. Before the sputtering, sample preparation has been done as it is mentioned. Substrates take their places on the substrate holder, and vacuum was started. Once they take the places, the holder was kept fixed. The pressure during the sputtering process was kept at 3mTorr by controlling the conductance with the gate valve between the chamber and the pumping system. The deposition rates can be controlled separately by changing the power of the target and temperature of the heater. In this work, only the SiO₂ target was fixed (180 W), and applied DC power to the Ge target was varied to control the Ge content (6 W, 8 W, and 10W, respectively) in the film.

3.1.4 In-situ Annealing During The Deposition

During deposition process was occurring, the heater works so that in-situ annealing during the deposition was achieved. Temperature of the heater has been increased gradually not to cause any thermal shock. Each sample set has been heated at a specific deposition temperature which is room temperature (RT), 400 °C, 600 °C, and 800 °C, respectively. Table 3.1 summarizes all the experimental parameters about magnetron-sputtered and insitu annealed samples.

Table 3-1 Magnetron-sputtered and in-situ process samples data

P_{Ge} (W)	P_{SiO₂} (W)	Substrate Temperature (°C)			
6	180	RT	400	600	800
8	180	RT	400	600	800
10	180	RT	400	600	800

In this thesis, our aim was to investigate Ge crystallinity, structural evolution of Ge/SiO_x and Ge/GeO_x species, and their optical responses through ultraviolet-visible/near-infrared (UV-Vis/NIR), Rutherford back scattering (RBS), Raman and X-ray photoelectron (XPS) analyses. To define the nanocrystal structure, Transmission Electron Microscopy (TEM) and Scattering Electron Microscopy (SEM) images are also evaluated.

3.2 Characterization and Measurement Techniques

3.2.1 Raman Spectroscopy (RS)

Raman spectroscopy (RS) is a vibrational spectroscopic technique that can measure the crystallinity of solids [43]. There are several reasons to use this test method. One of the advantages of RS is that it is strain sensitive, so it can be used to measure stress in a semiconductor device and material. In small diameter, the light beam is focused, then the stress can be measured in small areas [44].

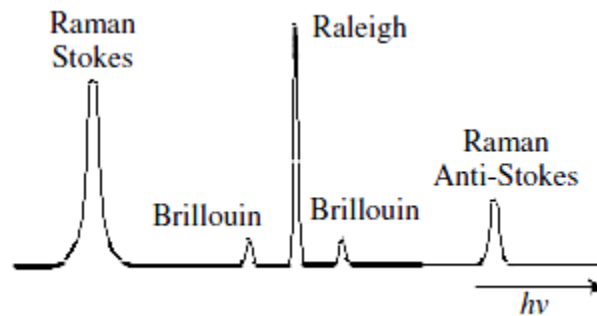


Fig 3-6 Scattered light energy distribution.

When light is scattered from the surface of a sample, mainly wavelengths of the scattered light is found to contain incident on the sample (Rayleigh scattering in Fig. 3.6); however a part of incident light interacts with the material at different wavelengths after scattering. Raman scattering can be defined as the interaction of the incident light with optical phonons. Additionally, Brillouin scattering can be defined as the interaction of the incident light with acoustic phonons. Illustrated in Fig. 3.6, optical phonons have higher energies than acoustic

phonons. Thus, optical phonons give larger photon energy shift than acoustic ones. [45].

In Raman effect, when the incident photon gives energy to the lattice in the form of a phonon, known as phonon emission, and then this incident photon becomes as a lower energy photon. This frequency shift is named Stokes-shifted scattering. On the other hand, the incident photon absorbs a phonon, then it becomes with higher energy. This situation is called anti-stokes shifted scattering which is shown in Fig. 3-6 as energy distribution of scattered light [44].

During Raman spectroscopy measurements, a laser pump is incident on the sample. A photo detector detects scattered light from the samples. Then, in the Raman microprobe, a laser whose pump is bright and monochromatic in order to separate the signal from the laser pump illuminates the sample through a commercial microscope. Detection is difficult by the weak signal against an intense background of scattered pump radiation. If the Raman scattering is observed at correct angles to the pump beam, the signal to noise ratio can be enhanced [45].

In this thesis study, backscattering Raman measurements were performed with Jobin Yvon Horiba confocal micro-Raman at room temperature at GÜNAM Measurement Laboratory. As an excitation source, He-Ne laser with 632.83 nm was used. Also, double mono chromator and Peltier cooled charge-coupled device (CCD) detector with a resolution less than 1 cm^{-1} was used to detect Raman shifts.

3.2.2 Transmission Electron Microscopy (TEM)

The TEM is a technique which gives detailed information on the structure of nanostructures. The TEM produces a transmitted electron image of a thin specimen, magnified from 100 to approximately 500,000 times, and with a resolving power of approximately 0.2 nm[46]. To produce the standard bright-field TEM image, the electron beam must be able to penetrate the sample with many electrons which are transmitted through the sample. The quality of the

image in the TEM depends not only on the expertise of the microscopist, but also on the on the quality of the specimen preparation for the TEM.

By using the TEM imaging method, nanocrystals' shape, size distribution, density and location in the matrix can be measured. Thus, in this thesis, energy filtered TEM (EFTEM) images can be seen.

TEM pictures were taken of University of Catania within the frame work of a joint project.

3.2.3 X-Ray Photoelectron Spectroscopy (XPS)

X-Ray Photoelectron Spectroscopy is a destructive, surface analysis technique which gives the information about the atomic composition of the surface and chemical environments, i.e. binding states (oxidation states) of the elements [47]. Surface analysis by XPS, more commonly known as electron spectroscopy for chemical analysis (ESCA), is accomplished by irradiating a sample with monoenergetic soft x-rays and energy analyzing the electrons emitted [48]. Thus, atomic core levels are excited by the incident x-ray beam to produce photoelectrons. Then, the energy spectrum of those particles is monitored via an electrostatic analyzer. In this way, it is possible to determine small shifts in the core levels or the valence band of the atomic assembly in order to assess the chemical state of the probed atoms with a suitably small energy spread in the incident x-ray beam. In that case, the photo electron escape depth defines the thickness of the analyzed layer in a sample [49].

All measurements were performed in the Central Laboratory at METU via Specs Lab XPS system.

3.2.4 Ultraviolet-visible Spectroscopy (UV-VIS)

Ultraviolet-visible spectroscopy means the absorption spectroscopy or reflectance spectroscopy in the ultraviolet-visible spectral region. Thus, it uses light in the visible and adjacent (near-UV and near-infrared [NIR]) ranges. In this region of the electromagnetic spectrum, molecules are exposed to electronic transitions. Then, transition is measured by the movement of molecules from the excited state

to ground state, while absorption is measured transitions from the ground state to the excited state [50].

In this thesis, optical measurements were done by UV-Vis spectroscopy. This gave the transmittance and reflectance analyses, and also band gap.

UV-Vis spectroscopy measurements were taken of University of Catania within the frame work of a joint project.

3.2.5 Rutherford Backscattering Spectroscopy (RBS)

Rutherford backscattering spectroscopy, also known as high-energy ion (back) scattering spectroscopy (HEIS), is basically based on backscattering of ions incident on a sample [51]. A sample is bombarded with energetic ions and measuring the energy of backscattered He ions. It allows determination of the masses of the elements in the sample, and by using it their depth distribution over distances from 10 nm to a few microns from the surface, their areal density, and the crystalline structure in non-destructive manner. A schematic view of RBS technique is given in Fig. 3.7.

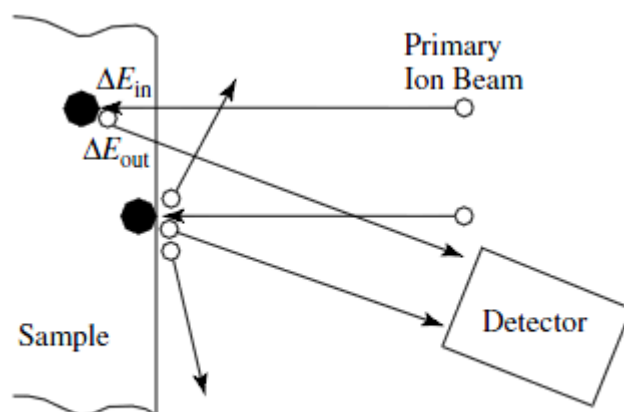


Fig 3-7 Rutherford backscattering schematic.

RBS can provide not only atomic composition but also depth scales to accuracies of 5% or better. The detection limit is 10^{17} to 10^{20} cm^{-3} , but depends on the

element and on energy of ions. The sensitivity to light elements, e.g. oxygen, carbon, and nitrogen, in the presence of heavier elements is poor. Therefore, experimental techniques such as detector angle changes beam tilting, and incident energy variations should be applied in this technique.

In this thesis, RBS is used to define atomic concentration variations of Si, Ge, O. All measurements were carried out at University of Catania, Italy.

3.2.6 Scanning Electron Microscopy (SEM)

Scanning electron microscopy, SEM, is a sort of electron microscope that generates images of a sample. In order to do so, the sample is scanning with a beam of electron which is focused by electron microscope. When the electrons from electron microscope interact with atoms in the sample, the signals from the electron source can be detected

Most techniques for the preparation of the samples for the SEM are easier than for the TEM due to the examination the whole surface of samples. Also, no sectioning is required in the SEM. Besides, SEM has a large depth of field. When we compare a light microscope, its depth of field can be up to five hundred times greater than that of a light microscope. The total information content of the image from an SEM can be very executed because of its great depth of field [46].

In this study, SEM is mostly used to measure the thickness of the thin film deposited by magnetron sputtering technique. In a conventional SEM system, the electron gun produces a beam of electrons that is attracted through the anode and condensed by the condenser lens, and then focused as a very fine point on the specimen by the objective lens. Then, the beam is scanned on the surface of the specimen, and for the imaging process, secondary electrons which are emitted from the sample surface are collected by e detector.

SEM measurements were taken of University of Catania within the frame work of a joint project.

3.2.7 Current-Voltage Measurements (I-V Measurements)

For the device characterization and operation, the electrical properties are very important. One the most significant parameters in this manner is the resistivity of the film. It can be obtained by measuring the film resistance from the surface using a configuration as illustrated in Fig. 3.8.

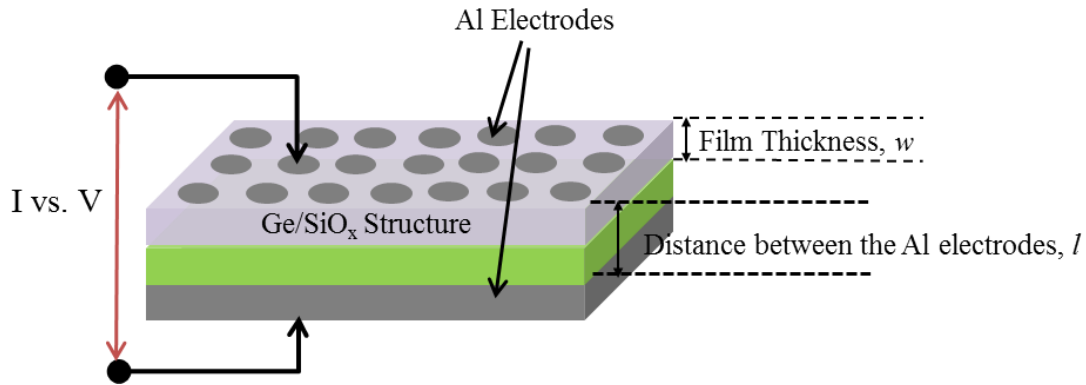


Fig 3-8 Simple I-V measurement schematics.

After the I-V characteristics measurement, the resistance between two electrodes can be obtained by using Ohm's law. Then, from the following formula, the resistivity can be calculated,

$$\rho = \frac{RA}{l} \quad (3.1)$$

where ρ is the resistivity, A is the path that electrons take after excited, and R is the calculated resistance. Thus, A can be the multiplication of width of the substrate and thickness of the thin film. l is the distance between the metal contacts.

In this thesis, since the Si substrate is p-type, metal contacts are Aluminum at the top of the samples and the bottom side of the samples as shown in Fig. 3.9.

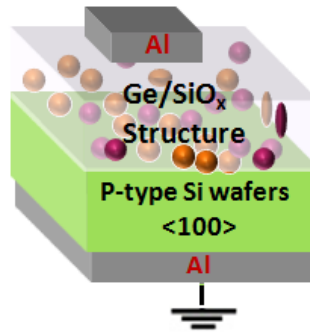


Fig 3-9 Schematic view of a specimen used in I-V measurement.

In this study, for I-V measurements, a Keithley 2400 Sourcemeter system has been used. The dark-light properties have been investigated via an Oriel AM 1.5G solar simulator which is available at GÜNAM facility.

CHAPTER 4

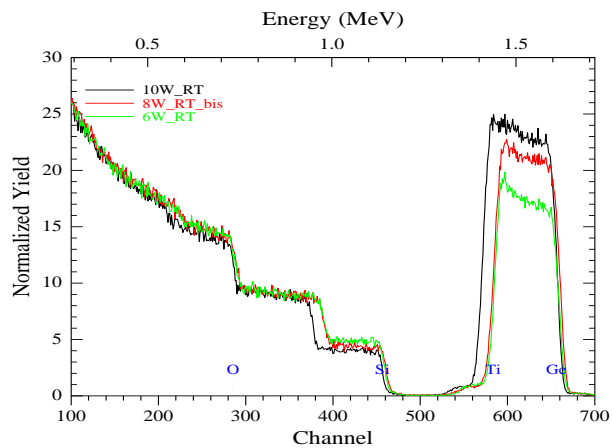
RESULTS AND DISCUSSION

4.1 Properties of as-deposited and deposited samples

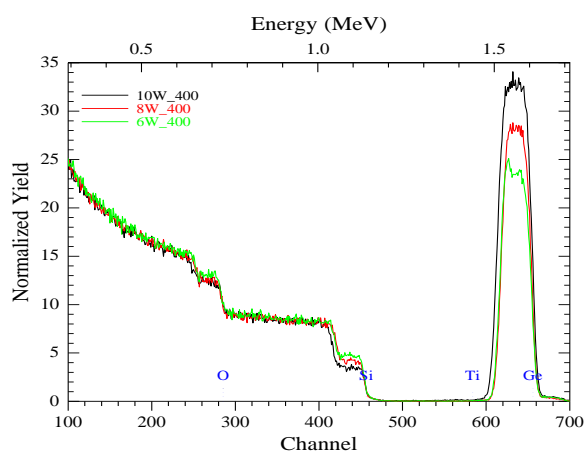
In this study, our aim is to produce interconnected, sponge-like Ge nanostructures embedded in SiO₂ matrix using co-sputtering technique. Our main goal is to create a structure having both quantum confinement and easy transport channel as an electrical transport property.

To achieve this aim, the excess amount of Ge content has been tried to optimize in the matrix. Hence, the applied power of the Ge target was increased gradually from 6W to 10W at DC power supply, while applied power of SiO₂ target was fixed at 180W at RF power supply. Three different powers were applied to the Ge target: 6, 8, 10W. Also, to investigate the temperature effect, samples were deposited at different temperatures; i.e. room temperature (RT), 400 °C, 600 °C, and 800 °C. Since all the film vaporized at 800 °C, there was observed no film formation at that temperature.

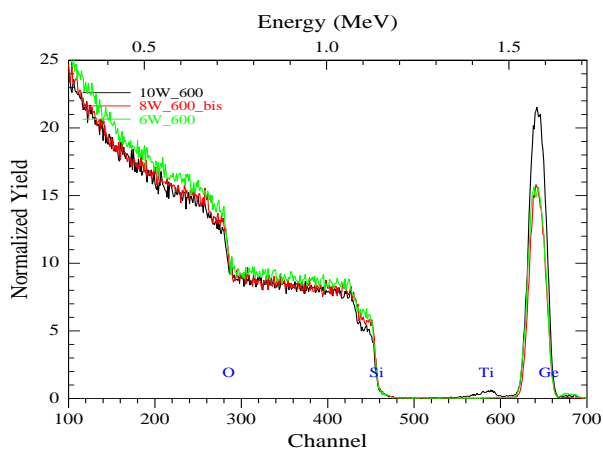
Firstly, RBS and SEM measurements have been performed to determine the composition of the materials. Fig. 4.1 and Fig. 4.2 show RBS of the samples deposited with various powers.



(a)

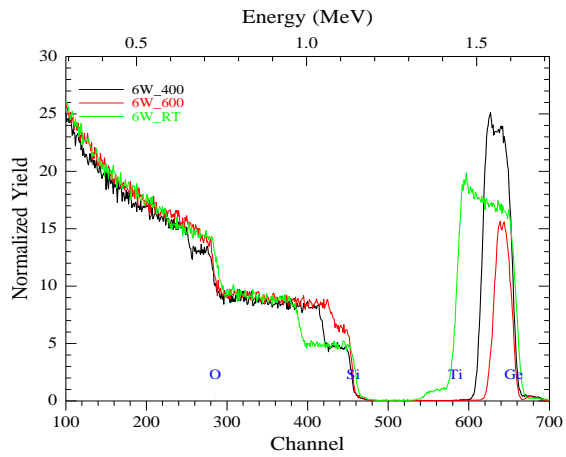


(b)

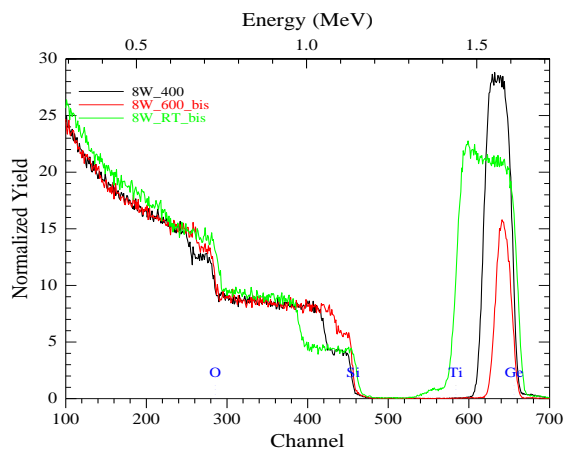


(c)

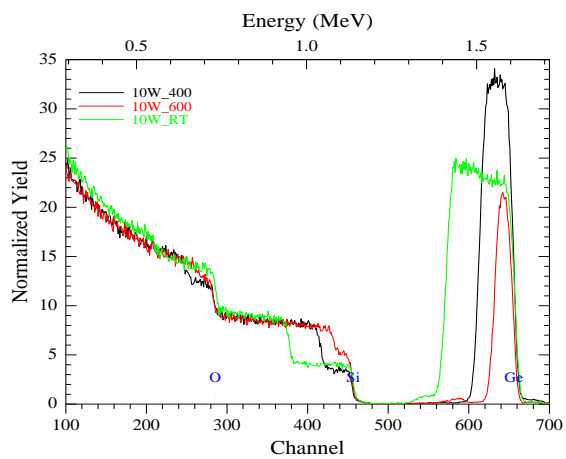
Fig 4-1 RBS results of Ge/SiO_x samples (a) As deposited samples, (b) 400 ° annealed samples (c) 600 ° annealed samples.



(a)



(b)



(c)

Fig 4-2 RBS results of Ge/SiO_x samples (a) The applied power of Ge 6W, (b) The applied power of Ge 8W (c) The applied power of Ge 10W.

In Fig 4.1(a), the power of Ge target is compared; then composition of Ge concentration is compared for the as deposited samples. The same study is also seen for 400 °C, and 600 °C annealed samples as shown Fig. 4.1 (b) and (c). It can be interpreted that the thicknesses of 10W and 8W deposited samples are very close to each other. Then, to observe the temperature effect, the graphs in Fig. 4.2 have been plotted. In each power, the annealed samples at 400 °C show maximum Ge content. This is expected because there occurs an evaporation while deposition due to composition of GeO₂ at high temperature. That's why the thickness of the sample includes the same Ge concentration for 6W, 8W, or 10W in 600 °C annealed is lower than 400 °C annealed.

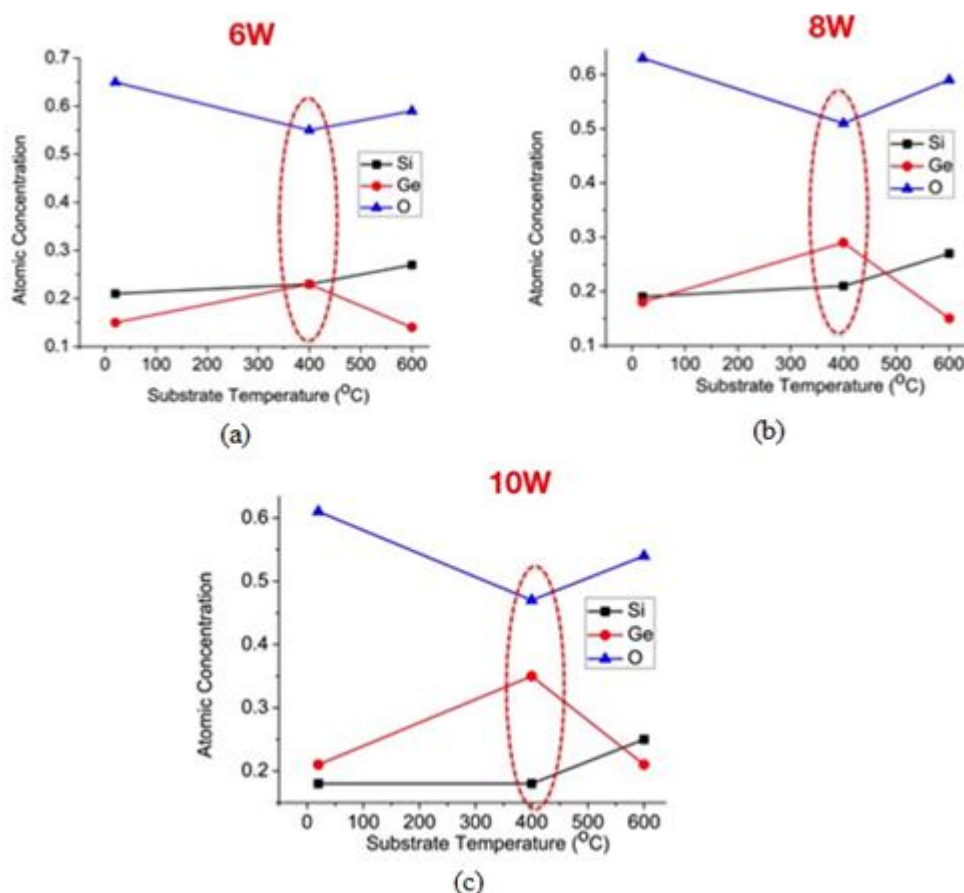
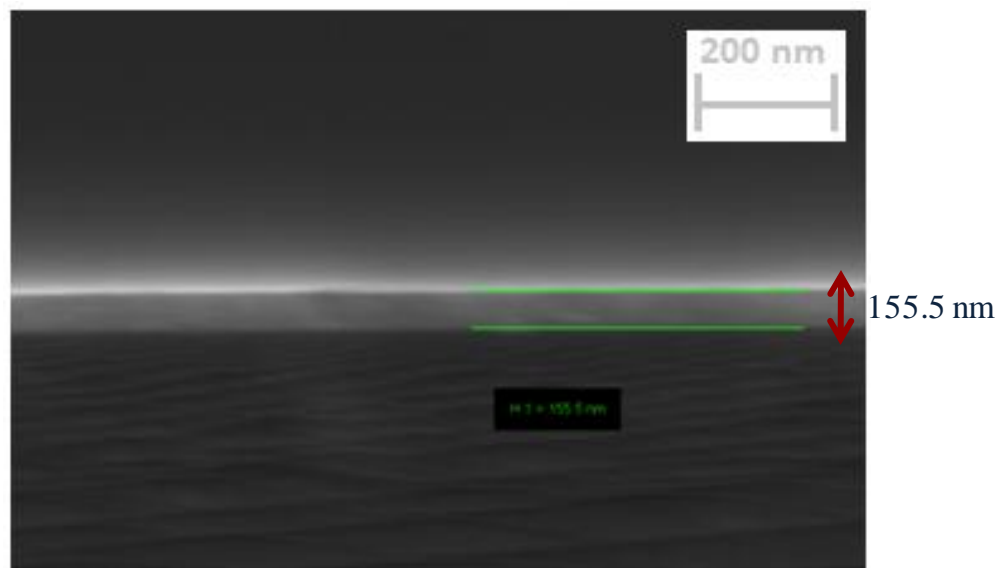


Fig 4-3 RBS elemental results of Ge/SiO_x and Ge/GeO_x samples with the applied power of Ge (a) 6W, (b) 8W and (c) 10W, the substrate temperature VS atomic concentration.

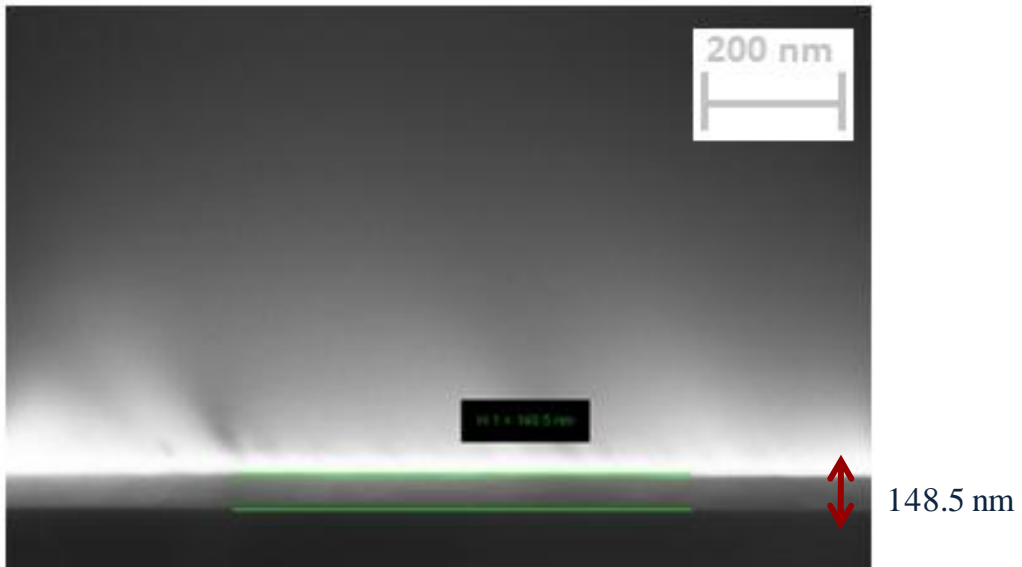
The atomic concentration (Fig. 4.3) has been plotted regarding the values in Fig. 4.1 and Fig. 4.2. It shows that Ge concentration is increased with respect to Si concentration at 400 °C. Further increase in temperatures leads to an abrupt decrease in Ge concentration. It means that Ge disappears at this temperature. The same temperature effect is also seen in Fig. 4.3. It is clearly seen in all graphs that after 400 °C annealing, Ge concentration is decreasing while the temperature is increasing. Therefore, 400 °C can be seen as a transition stage from the point of Ge concentration.

Besides RBS analysis, SEM measurements have been taken to measure the film thicknesses. Cross-sectional SEM images of in-situ process at 400 °C and 600 °C samples are shown in Fig. 4.4 and Fig 4.5.

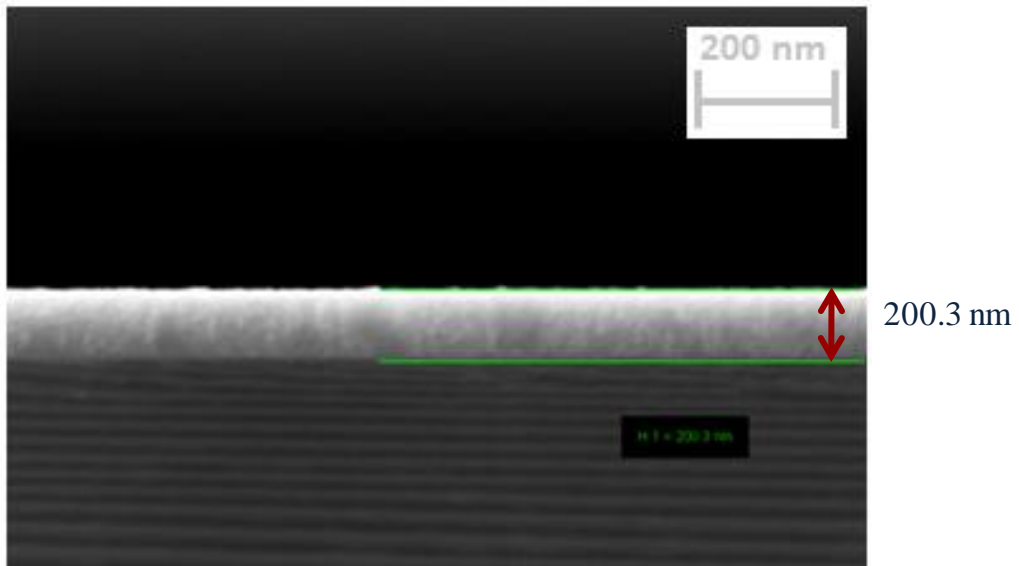


(a)

Fig 4-4 SEM images of the samples deposited in-situ process in 400 °C with applied power (a) 6W, (b) 8W, and (c) 10W.

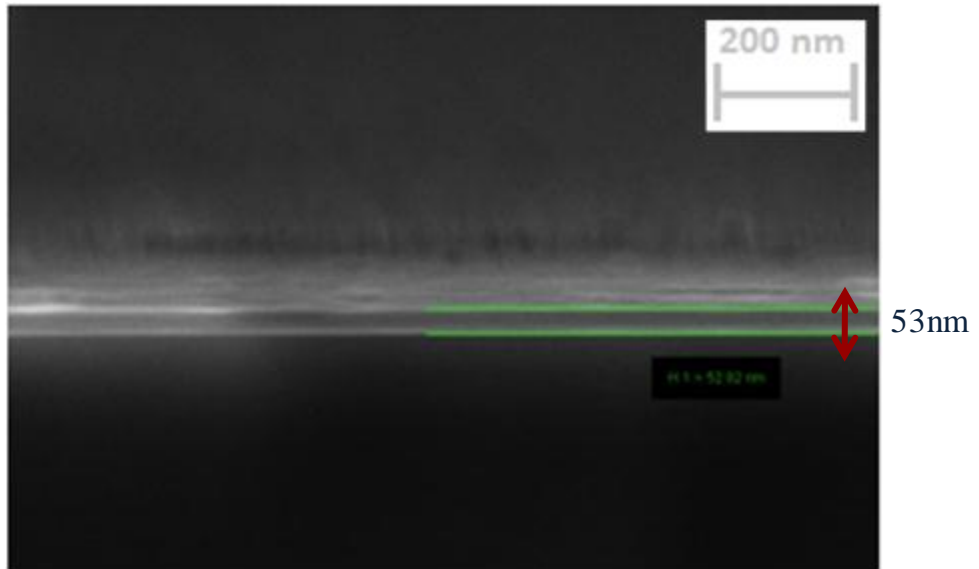


(b)

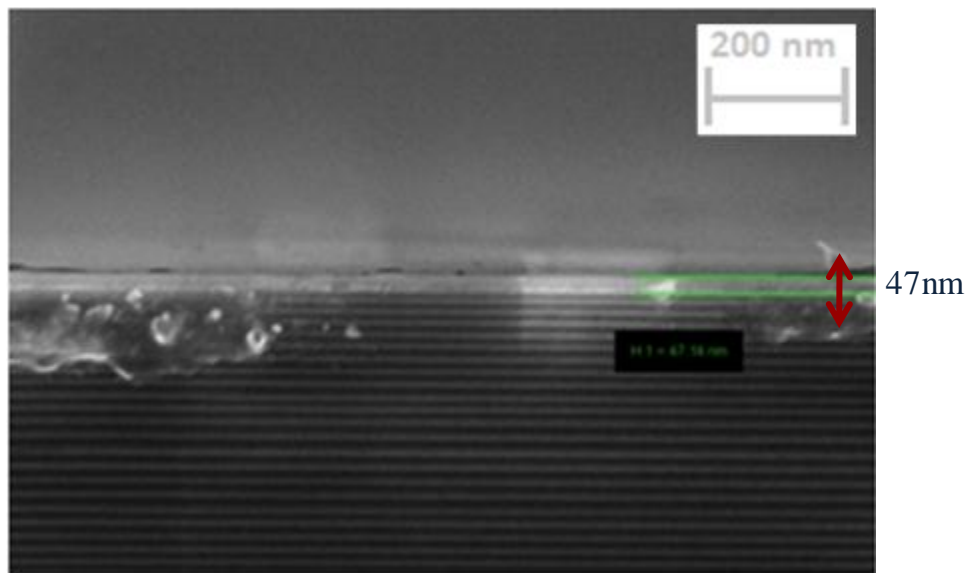


(c)

Fig 4-4 SEM images of the samples deposited in-situ process in 400 °C with applied power (a) 6W, (b) 8W, and (c) 10W (continued).

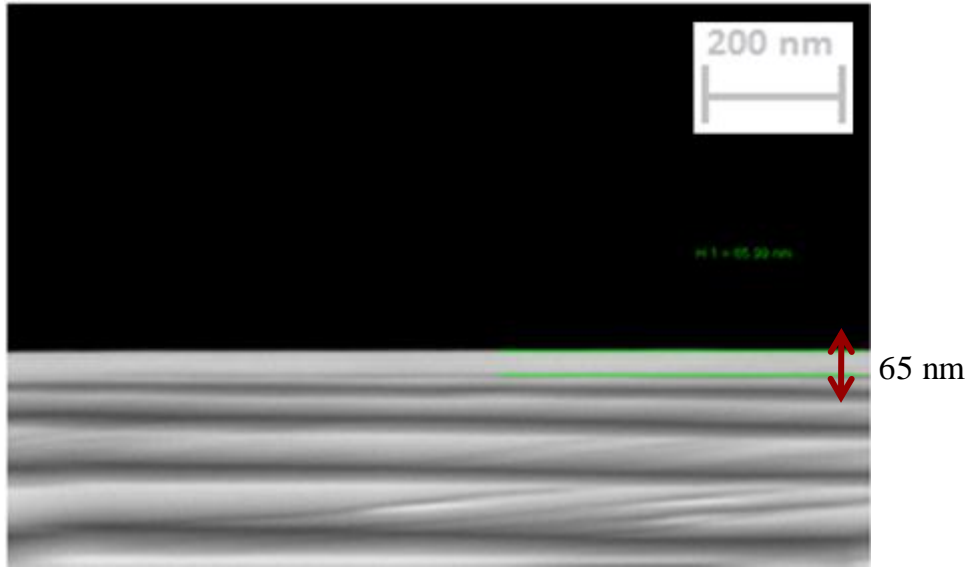


(a)



(b)

Fig 4-5 SEM images of the samples deposited in-situ process in 600 °C with applied power (a) 6W, (b) 8W, and (c) 10W.



(c)

Fig 4-5 SEM images of the samples deposited in-situ process in 600 °C with applied power (a) 6W, (b) 8W, and (c) 10W (continued).

The thicknesses are 155.5 nm, 148.5 nm and 200.3 nm for the samples deposited with 6W, 8W, and 10W at 400 °C in-situ process, respectively as shown in Fig. 4.4. SEM images confirm the thicknesses of the deposited films from the RBS results. It was mentioned about an overlap in RBS results for the 8W and 10W deposited samples. When we look at the thicknesses at the SEM images, again, it is seen. Since the thickness values are so close to each other, RBS measurements gave these results. Similar situation is also seen in Fig. 4.5 which affirms the RBS results from the samples deposited at 600 °C with applied power 6W, 8W and 10W respectively. The thicknesses change also depending on the annealing temperature as it is mentioned before. All these RBS and SEM results reveal that applied Ge concentration and annealing temperature are important parameters that determine the thin film composition.

4.2 Ge crystallization during in-situ annealing

In order to verify the crystalline structure of the deposited films, Raman Spectroscopy (RS), and Energy-Filtered Transmission Electron Microscopy (EFTEM) have been performed.

4.2.1 Transmission Electron Microscopy

During TEM measurements, nanocrystals' shape, density, size distribution and location in the matrix have been measured. Because any TEM measurement requires extremely careful sample preparation steps and high operation cost, analysis of all samples could not be possible. Only the applied power 10W (RT, 400 °C, 600 °C) samples have been measured as shown in Fig.4.6, Fig. 4.7, Fig. 4.8, respectively.

After giving the detailed information about TEM measurements, results of optical analyses are presented.

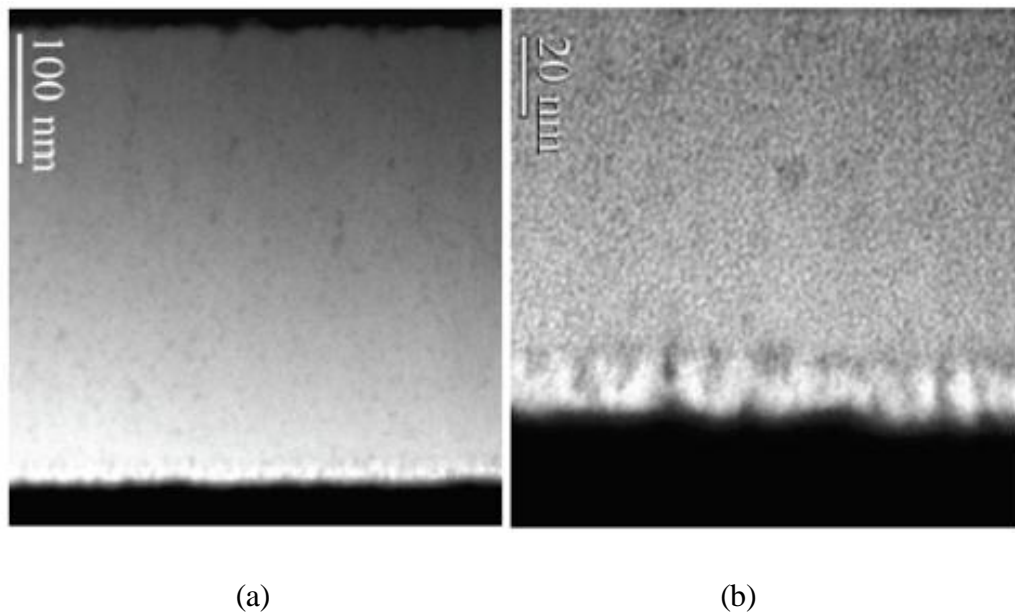


Fig 4-6 EFTEM images of 10W RT deposited Ge/SiO_x thin film a) Thin film image on Si Substrate b) The interface of Si substrate and thin film.

In Fig. 4.6(a), as sputtered sample's EFTEM image is shown. The dark region shows the Si substrate, and the bright region shows the thin film which includes Ge/SiO_x structure. In Fig. 4.6(b), when it is zoomed in to the picture, there appears an amorphous structure between the film and the substrate. That amorphous structure is a place where we observed Ge accumulation.

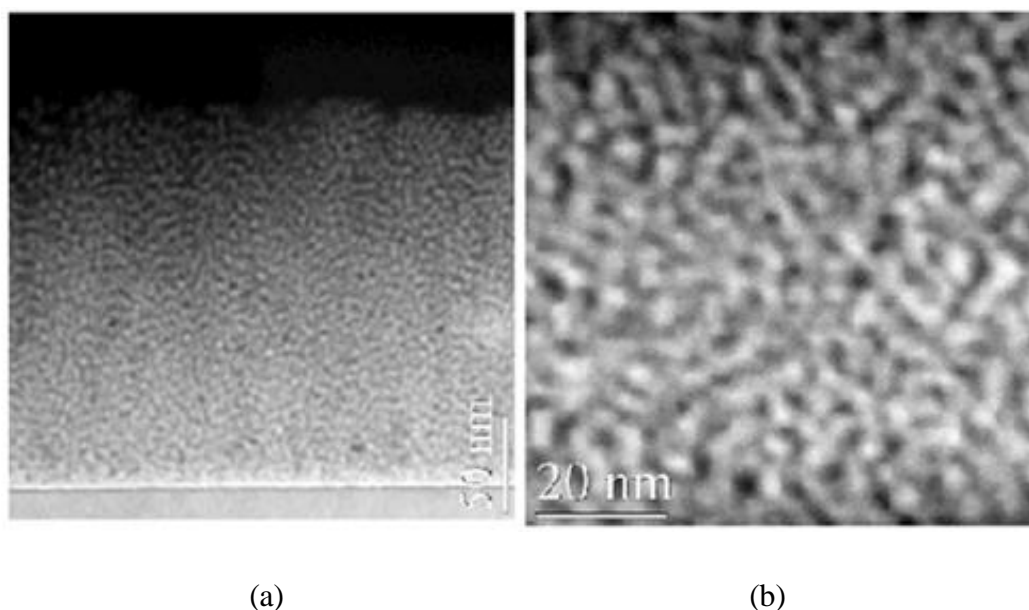


Fig 4-7 EFTEM images of 10W at 400 °C deposited Ge/SiO_x thin film a) Thin film image on Si Substrate b) The interface of Si substrate and thin film.

In Fig. 4.7(a), there are shown an EFTEM image of the samples deposited at 400 °C with applied power 10W by magnetron sputtering technique. In this case, the gray region shows the Si substrate, and the bright region shows the thin film which includes Ge/SiO_x structure. It is clearly seen from the image that the thickness of the thin film is decreased in comparison with deposited at RT one. It is expected because while in-situ process, some of Ge disappears in the form of GeO₂. In Fig. 4.7(b), when it is zoomed in to the picture, there appears a long-range order that is needed for crystallization.

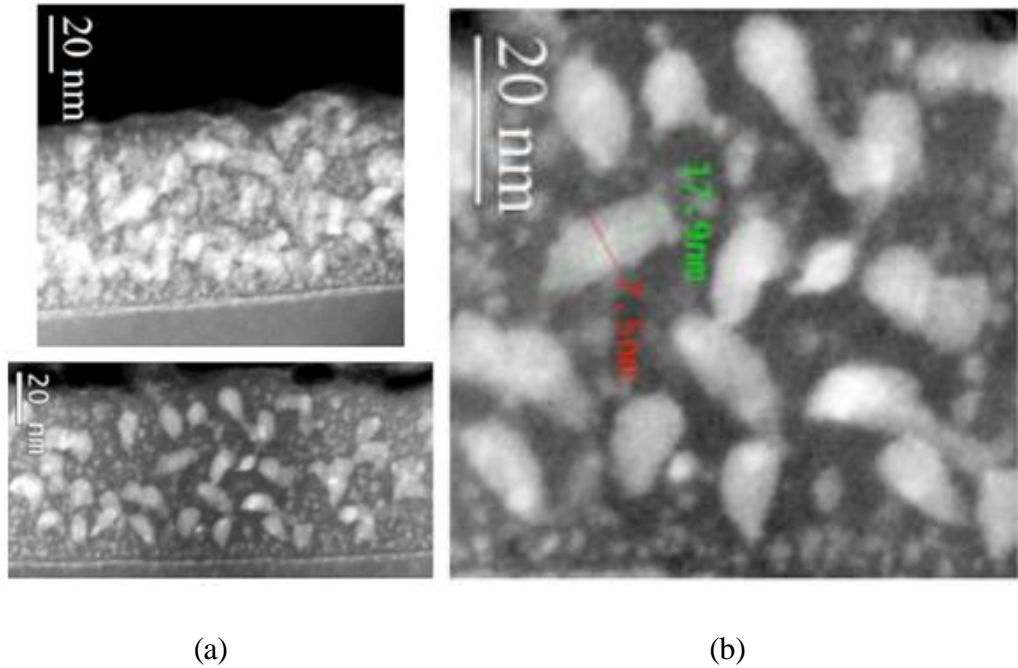


Fig 4-8 EFTEM images of 10W at 600 °C deposited Ge/SiO_x thin film a) Thin film image on Si Substrate b) The interface of Si substrate and thin film.

In Fig. 4.8(a), the EFTEM images of the samples that are deposited 600 °C in-situ process with an applied power 10W by magnetron sputtering technique are shown. The gray region shows the Si substrate, and the bright region shows the crystallized Ge. The thickness of the thin film reached its minimum value due to evaporation as GeO₂. On the other hand, increasing temperature causes a decrement in the defects in thin film. In Chapter 2, quantum confinement effect was explained. To get discrete energy levels, one can compare the radius of nanocrystals with the Bohr Radius. Depending on their energy, the electrons orbit only certain distances from the nucleus according to Bohr Model. When the hydrogen atom, the simplest one, is thought, Bohr Radius could be defined as the place of nearest electron to the nucleus with the lowest energy. When it is looked at Fig. 4.8(a) in detail (in Fig. 4.8b), bright spots reveal noticeably the crystallization of Ge. In Fig. 4.8(b), the radius of crystal dimension is determined the lower than critical Bohr radius for Ge which provides the conditions that is necessary for quantum confinement.

There is observed no film formation in all the samples that are deposited at 800 °C in-situ process. Hence, they are not included in this work.

4.2.2 Band Gap Estimation

Optical analyses starts with UV-Vis/NIR spectroscopy measurements. UV-visible spectroscopy is used to determine transmission and reflection characteristics of the samples. Therefore, transmittance and reflectance analyses have been done via UV-visible spectroscopy. Additionally, optical band gap (E_g) determination of the samples have been done by using well-known Tauc's equation [51-52]:

$$\alpha h\nu = B(h\nu - E_g)^{1/2} \quad (4.1)$$

In this equation, $h\nu$ is incident photon energy, B is the edge width parameter related to the width of band tails and density of states in the film, and α is the absorption coefficient. The absorption coefficient of α is defined by $I(z)=I_0e^{-\alpha z}$, where $I(z)$ is the flux density if incident light is I_0 , z is the distance measured from the incident surface, and in that case z is the thickness of thin film. I/I_0 is equal to transmission T . In this method, to get the Tauc's curves, $(\alpha h\nu)^2$ is plotted against $h\nu$. Main idea is to extrapolate the linear portion of the curve and its intercept with the energy axis is taken to represent the optical band gap [54]. Hence, the optical band gaps which are obtained from Tauc's plot are given in Fig. 4.10.

All the samples (as-sputtered, 400 °C, 600 °C) with an applied power 6W, 8W, and 10W, respectively, are utilized in UV-visible measurements. They are listed below:

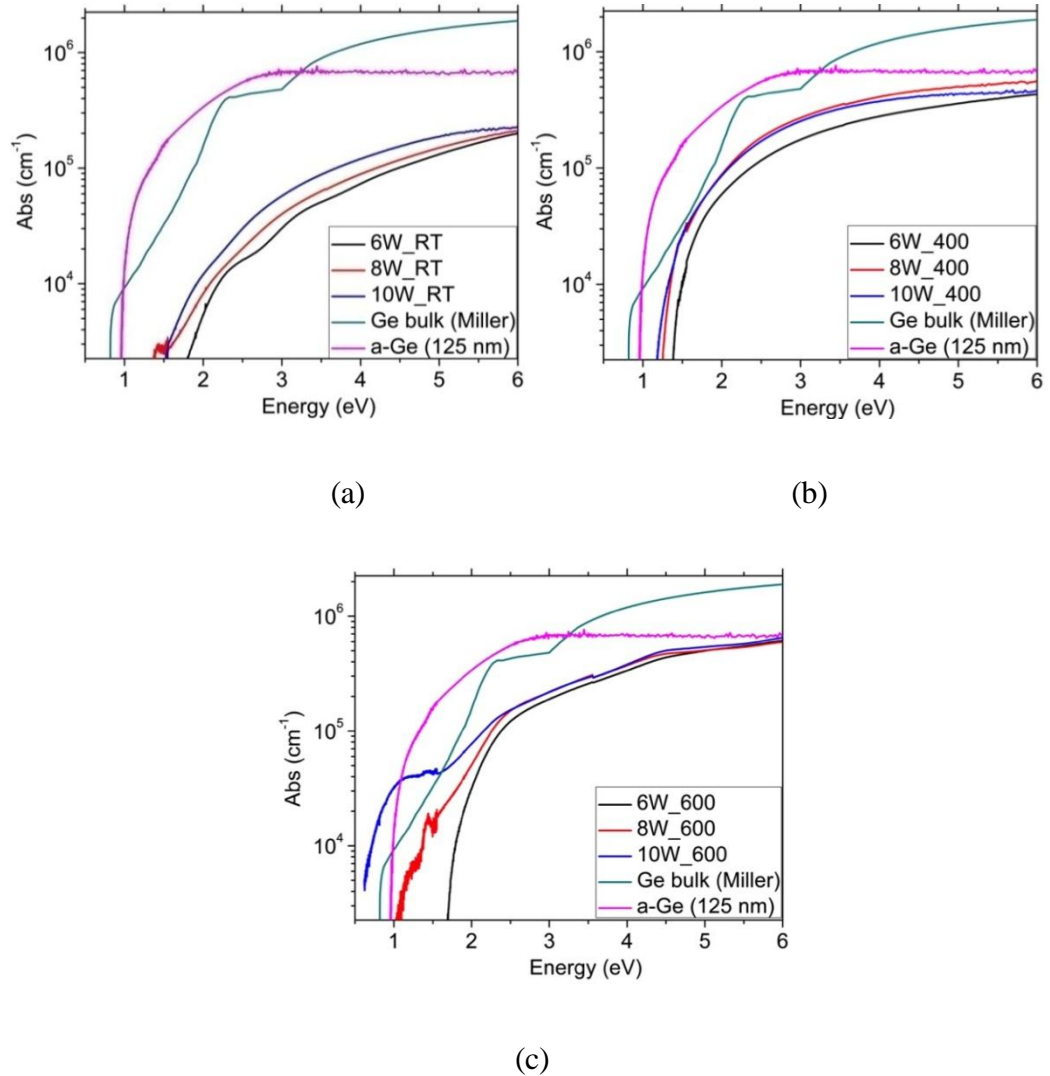


Fig 4-9 Ge concentration dependence of absorption coefficients at (a) RT, (b) 400 °C, and (c) 600 °C substrate temperatures.

The absorption curves of amorphous Ge and bulk-Ge which means it is crystal in that form are given in Fig. 4.9 (a, b, and c) to understand the crystallinity easily. In Fig. 4.9(a), as-deposited ones are included and they are all in amorphous form. In Fig. 4.9(b), 400 °C samples are shown. The applied power 6W deposited sample is amorphous phase. However, crystallinity starts at the applied power 8W and 10W in the Fig. 4.9(b), since behavior of the curve is pretty similar to the bulk-Ge one. As shown in Fig. 4.9(c), it is clearly seen that Ge is crystallized well

at 600 °C for 10W ever for 8W as well. On the contrary, 6W is again in amorphous form. These results are coherent with TEM results because we have seen crystallinity with 10W applied power deposited at 600 °C as in the previous section.

Optical band gap values have been calculated through Tauc's plots by using UV-visible spectrometer. It is seen in Fig. 4.10 and Table 4.1.

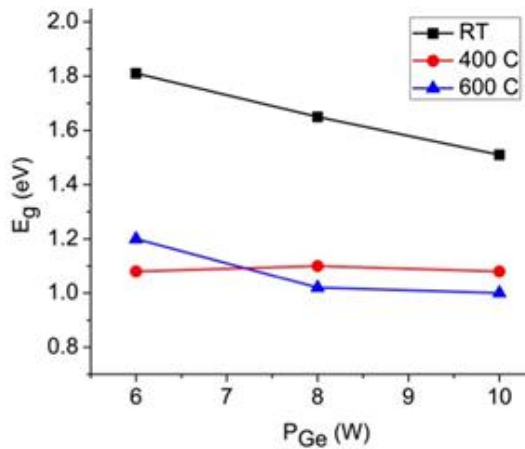


Table 4-1 Optical band gap values.

Sample	E_g (eV)
6W_RT	1.81
8W_RT	1.65
10W_RT	1.51
6W_400C	1.07
8W_400C	1.11
10W_400C	1.08
6W_600C	1.24
8W_600C	1.02
10W_600C	1

Fig 4-10 Change in optical band gap with respect to the Ge concentration at different substrate temperatures.

As shown in Fig. 4.10, at RT, when the applied power of Ge to the substrates is increasing, optical band gap of the samples is decreasing. In other word, there is change from 1.8 eV to 1.55 eV. This situation indicates that the samples prepared at room temperature show quantum confinement effect. However, the other samples at deposited at 400 °C and 600 °C do not show a major change in optical band gap values. Hence, it can be thought those samples do not indicate presence of quantum confinement effect.

4.2.3 Raman Spectroscopy

Raman spectroscopy is used to understand the crystallization process. Ge-Ge bond vibrations are monitored to get information on phase change of Ge from amorphous to crystalline state.

All the samples have been investigated by RS. Fig. 4.11 shows Raman spectra of the as-sputtered and in-situ process samples.

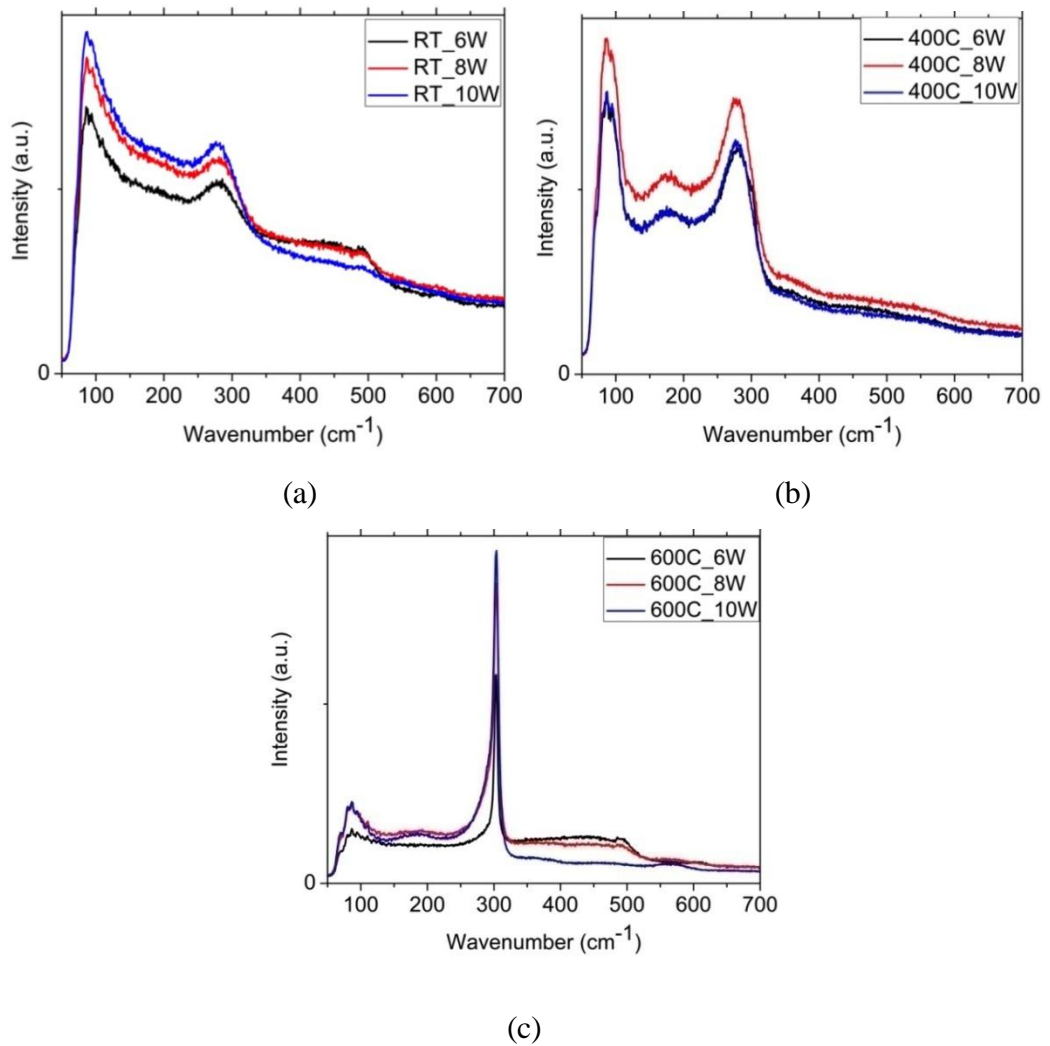


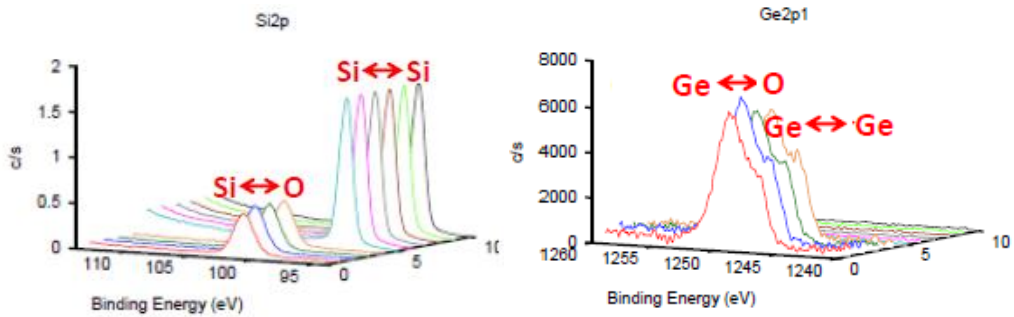
Fig 4-11 Ge concentration and substrate temperature dependence of Raman spectra (a) RT, (b) 400 °C, and (c) 600 °C.

As shown in Fig. 4.11(a), as-sputtered samples show no indication of nanocrystal formation at any applied power of Ge. It can be seen a broad band which is the characteristic feature of amorphous Ge in Fig 4.11(a)[55]. However, when the applied temperature is increasing, a sharp Raman peak is observed which is indicating Ge crystallization [56]. The Raman spectrum exhibits a Lorentzian line at 300 cm^{-1} with an intrinsic width of around 3 cm^{-1} for bulk crystalline Ge. The reason of the shift and asymmetrical broadening of the Raman spectra is due to the confinement of phonons and this is also characteristic of nanocrystals [56-57]. In Fig. 4.11(b), it is clearly seen that formation of Ge crystallization starts around 299 cm^{-1} . And then, a sharp peak is caught in Fig. 4.11(c). This means that Ge crystallinity increases with the increase of annealing temperature. Generally, when the annealing temperature increases and reaches a threshold level, then the partial structure of the as-deposited film transforms from amorphous phase to crystalline phase [59]. Additionally, when the annealing temperature increases further, then more of the amorphous structure in the as deposited film is transformed into crystalline structure which is reflected in the intensity of the Raman peak [60]. Therefore, the threshold value in that work is said to be $400\text{ }^{\circ}\text{C}$ for the temperature. That also explains the increase in optical band gap at $400\text{ }^{\circ}\text{C}$.

4.3 Variations with Ge content

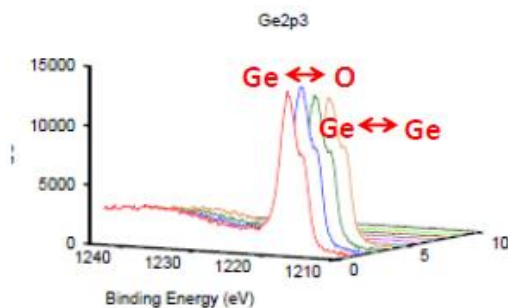
In order to determine film composition and chemical binding energies, X-ray photoelectron spectroscopy (XPS) has been used. XPS is operated to reveal the chemical states of the interface, and also to investigate the depth distribution of elements and their chemical states. XPS is also used to characterize physical-chemical properties of nanostructures.

The samples with the applied power of Ge are 10W have been studied in XPS measurements. The substrate of these samples is c-Si wafer as it is mention in the Chapter 3. During XPS measurements, thin film was etched until the substrate gradually. Because the only applied power of Ge being 10W samples are used, XPS results indicate that the stoichiometry of the system can be tailored by changing the temperature. Fig. 4.12 shows the results of XPS measurements.



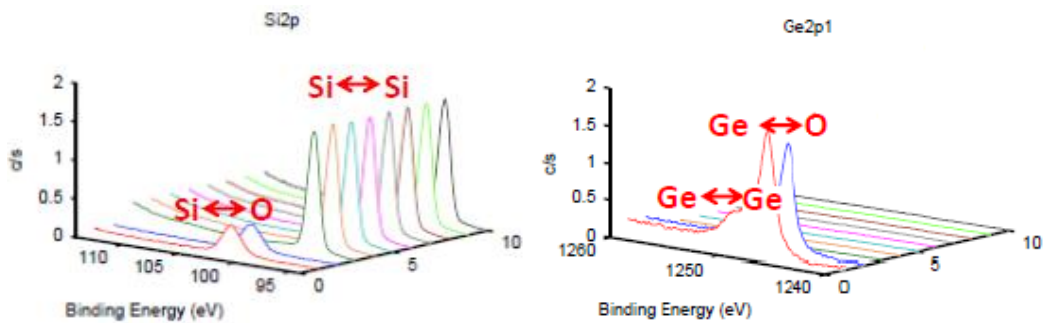
(a)

(b)



(c)

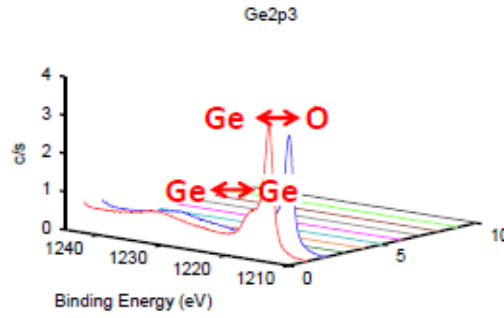
Fig 4-12 XPS spectra of (a) Si:2p, (b) Ge:2p¹, and (c) Ge:2p³ for 10W-RT sample.



(a)

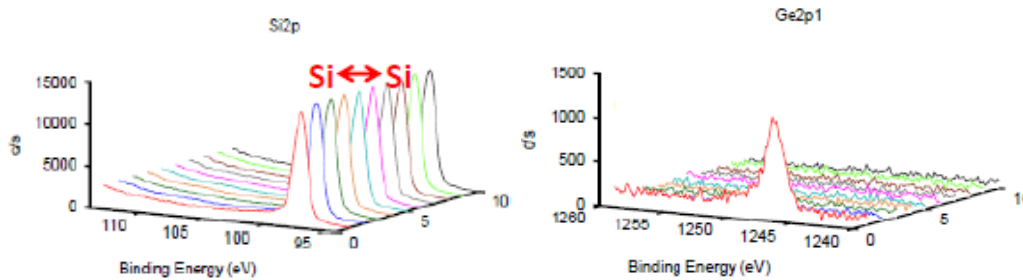
(b)

Fig 4-13 XPS spectra of (a) Si:2p, (b) Ge:2p¹, and (c) Ge:2p³ for 10W-400 °C.



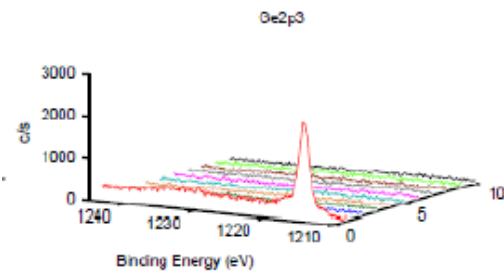
(c)

Fig 4-13 XPS spectra of (a) Si:2p, (b) Ge:2p¹, and (c) Ge:2p³ for 10W-400 °C (continued).



(a)

(b)



(c)

Fig 4-14 XPS spectra of (a) Si:2p, (b) Ge:2p¹, and (c) Ge:2p³ for 10W-600 °C sample.

As it was mentioned before, XPS depth profile analysis has been performed for determination of the Ge, Si and O distribution through the film structure. XPS depth profile analyses show a homogenous distribution of Si and Ge throughout the film. It can be seen that at RT Si is only bonded to O and Ge demonstrates both Ge-Ge and Ge-O bonds, where the latter is prominent in shown in Fig. 4.12 (a), (b) and (c). On the other hand, when temperature increases, Ge-Ge bonds

dominated the spectra (in Fig. 4.13(a), (b), and (c); in Fig. 4.14(a), (b), and (c)), which indicates strong Ge crystallization. It is also seen that the temperature increase leads to a diminished film thickness due to the fact that most Ge has become volatile GeO_2 and vaporized during the deposition as it is mentioned in TEM measurements.

4.4 Electric properties of devices made on Ge nanostructures

One of the most important properties is film conductivity which identifies materials. To form contacts on the devices, Al was evaporated on both side of the devices for Ohmic contact formation. Only the applied power of Ge 6W, 8W, and 10W at RT samples give promising results which are shown in Fig. 4.15. The measurement is performed in ambient atmosphere at room temperature. The applied voltage values have been limited -5V and +5V.

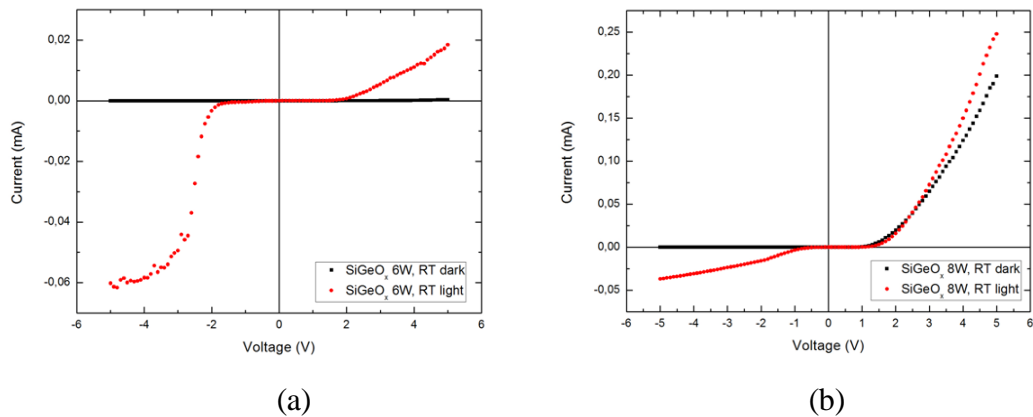
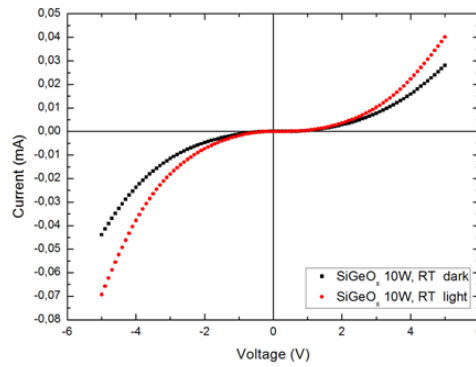


Fig 4-15 Measured Current-Voltage values of the samples with applied power of Ge (a) 6W (b) 8W (c) 10W at RT.



(c)

Fig 4-15 Measured Current-Voltage values of the samples with applied power of Ge (a) 6W (b) 8W (c) 10W at RT (continued).

In Fig. 4.15(a), the sample applied power of Ge 6W does not produce any photo current while it produces a very high photocurrent with high voltage under AM 1,5 G solar simulator. Similarly, in Fig. 4.15(b) and 4.15(c), of high voltage regimes, very high photo response can be obtained from the sample applied power of Ge 8W and 10W. When we compare the measurements both taken under dark and under light the 6W sample produces the highest photo response. However, if the positive region is analyzed, only the sample applied power of Ge 8W shows a better diode behavior. All these results show that our diodes are not consistent by producing typical diode properties.

All other samples (not shown here) also gave some remarkable response to the light. However, they do not give any current while the applied voltage is zero, used without illumination. Therefore, these devices could not work like a solar cell. The reasons while these devices give a promising response as a photodiode, but they could not work like a solar cell can be summarized as: The electric field which is created by the exposure of the positive and the negative space charge in the depletion region could not provide proper conditions. Namely, created electron-hole pairs recombine in the depletion region. On the other hand, when a high voltage is applied, these charges separate, and reach the surface. And then

they create a photo conductance. As a result of this, the graphs which are shown in Fig. 4.15 have been obtained from the I-V measurements.

CHAPTER 5

SUMMARY AND CONCLUSION

In this thesis, structural, optical and electrical characterization of Germanium nanostructures has been investigated for the possible optoelectronic and photovoltaic applications. To fabricate nc-Ge/SiO₂ thin film, physical vapor deposition technique (PVD) was used. In PVD, two magnetrons were used to sputter from SiO₂ and Ge targets at the same time. During the deposition, the heater was used to induce a crystalline structure. After the production period, for characterization of the samples, different diagnostic tools have been utilized. Basically, Raman Spectroscopy, absorption and transmission measurements, RBS, XPS, SEM and EFTEM image analyses were carried out to obtain detailed information about film characteristics. Moreover, to investigate the possibility of third generation solar cell applications, some conductivity measurements have been performed. In Chapter 2, theoretical back ground of this work was summarized. Nanocrystal and nanosponge structures for optoelectronic devices concepts are explained briefly in this chapter. The most important point in this section is that decreasing the dimension of nanocrystal particles leads to interesting properties including quantum confinement. To understand the confined nanostructures, quantum well, quantum wire, quantum dot concepts are explained using Schrödinger equation. Electrical and optical properties are described to interpret the results of the measurements. Finally, third generation solar cells based on Si nanocrystal are explained. In Chapter 3, description of experimental procedures used in this work is given. Firstly, necessary steps are given for the preparation of SiGeO layers by magnetron sputtering. And then,

working principles of the characterization techniques are examined. In Chapter 4, the results of the examined samples with various characterization techniques are presented. In order to understand the structural and optical properties of the deposited samples, properties of as-deposited and in-situ heated samples have been investigated. Besides, to understand the temperature effect, Ge crystallization during in-situ annealing has been explained. To examine the possibility for photodiode applications and the application of third generation solar cells, electric properties of devices made on Ge nanostructures were investigated.

In order to crystallize the samples, in situ process has been occurred with various temperatures. TEM results show that increase in temperature effects the nanocrystal Ge formation. Thus, while there is not observed any nanocrystal formation in the as deposited samples, when the temperature is applied at 400 °C nanocrystal formation starts. Furthermore, EFTEM images apparently reveal the nanocrystals achieved at 600°C. Then, controlling deposition rate with applied power to magnetrons, film thickness is controlled. RBS and SEM measurements indicate that the film thickness is increasing with increase power of applied to the Ge-magnetron source. However, increase in the temperature causes evaporation the thin film as GeO₂. Therefore, it has been confirmed that 400 °C is the transition temperature to deposite the thin film in order to start to obtain a crystalline structure. Raman spectroscopy also shows that most crystalline structure is obtained at 600 °C which is consistent with TEM measurements. Hence, increase in temperature really causes the formation of nc-Ge, but also evaporates the thin film. Then, electrical measurements have been performed to investigate the photodiode and possible photovoltaic applications. It has seen that the devices which are produced from magnetron sputtering in in-situ process technique are applicable for photodiode applications. Because the samples respond in light, but do not respond in dark, they are needed to develop for the photovoltaic applications.

In this study, Ge crystallinity, structural evolution of Ge/SiO_x and Ge/GeO_x species, and their optical responses were investigated. It is concluded that Ge crystallinity increases with increasing its concentration and substrate temperature. However, further increase in temperature led Ge to be vaporized thus temperature levels between 400 and 600 °C can be scrutinized for optimal conditions. Therefore, further studies can be performed regarding the increase crystalline structure in deposited films at 400 and 600 °C. We arranged the transition temperature is 400 °C, and by changing the applied power of Ge, the best structure can be obtained with regard to the crystallinity. That causes a better respond in photo diode applications, or even the third generation solar cell applications.

REFERENCES

- [1] C. Rao, P. Thomas, and G. Kulkarni, *Nanocrystals: Synthesis, Properties and Applications*. Springer, 2007.
- [2] T. Ihn, *Semiconductor Nanostructures: Quantum states and electronic transport*. 2010, p. 580.
- [3] S. . Benzer, *Phys. Rev. B*, vol. 70, p. 105, 1946.
- [4] P. N. Cheremisinoff, W. C. Dickinson, and 1980. 1-167., *Solar Energy Technology Handbook, Part A*. New York, NY: Marcel Dekker, Inc., 1980, pp. 1–167.
- [5] R. L. Bailey, *Solar Electrics Research and Development*, MI: Ann Ar. 1980, pp. 2–186.
- [6] B. J. Feldman, *An Introduction to Solar Cells*, vol. 48, no. 5. 2010, p. 306.
- [7] M. J. M. Pathak, J. M. Pearce, and S. J. Harrison, “Effects on amorphous silicon photovoltaic performance from high-temperature annealing pulses in photovoltaic thermal hybrid devices,” *Sol. Energy Mater. Sol. Cells*, vol. 100, pp. 199–203, 2012.
- [8] A. Luque and S. Hegedus, *Handbook of Photovoltaic Science and Engineering*. John Wiley and Sons, 2011, pp. 617–657.
- [9] G. P. Smestad, “Demonstrating Electron Transfer and Nanotechnology: A Natural Dye – Sensitized Nanocrystalline Energy Converter,” *J. Chem. Educ.*, vol. 75, no. 6, pp. 752–756, 1998.
- [10] J. Li, S. Kim, S. Edington, J. Nedy, S. Cho, K. Lee, A. J. Heeger, M. C. Gupta, and J. T. Yates, “A Study Of Stabilization Of P3HT/PCBM Organic Solar Cells By Photochemical Active TiO_x Layer,” *Sol. Energy Mater. Sol. Cells*, vol. 95, no. 4, pp. 1123–1130, 2011.
- [11] T. F. Schulze, Y. Y. Cheng, B. Fckel, R. W. MacQueen, A. Danos, N. J. L. K. Davis, M. J. Y. Tayebjee, T. Khoury, R. G. C. R. Clady, N. J. Ekins-Daukes, M. J. Crossley, B. Stannowski, K. Lips, and T. W. Schmidt,

- “Photochemical Upconversion Enhanced Solar Cells: Effect Of A Back Reflector,” *Aust. J. Chem.*, vol. 65, no. 5, pp. 480–485, 2012.
- [12] H. J. Möller, *Semiconductors for solar cells*. Artech House Boston, 1993.
- [13] M. A. Green, “The Future Of Crystalline Silicon Solar Cells,” *Prog. Photovoltaics Res. Appl.*, vol. 8, no. 1, pp. 127–139, 2000.
- [14] M. A. Green, “Crystalline And Thin-Film Silicon Solar Cells: State Of The Art And Future Potential,” *Sol. Energy*, vol. 74, no. 3, pp. 181–192, 2003.
- [15] J. Poortmans and V. Arkhipov, *Thin film solar cells: fabrication, characterization and applications*. Wiley, 2006.
- [16] A. G. Aberle, “Thin-Film Solar Cells,” *Thin Solid Films*, vol. 517, no. 17, pp. 4706–4710, 2009.
- [17] K. Pedersen, “Quantum Size Effects In Nanostructures,” no. 17, August, 2006.
- [18] T. P. Sidiki and C. M. S. Torres, *Silicon-Based Nanostructures*, vol. 3. 2000, pp. 233–289.
- [19] S. Sapra, J. Nanda, and D. D. Sarma, “Electronic Structure of Semiconducting Nanoparticles,” in *Encyclopedia of Nanoscience and Nanotechnology*, H. S. Nalwa, Ed. American Scientific Publishers, 2004, pp. 181–192.
- [20] S. Sapra and D. D. Sarma, “Electronic Structure and Spectroscopy of Semiconductor Nanocrystals,” in *Chemistry of Nanomaterials: Synthesis, Properties and Applications*, C. N. R. Rao, A. Muller, A. K. Cheetham, and Weinheim, Eds. Wiley-VCH, 2004, pp. 371–404.
- [21] A. Sharma, G. Sumana, S. Sapra, and B. D. Malhotra, “Quantum Dots Self Assembly Based Interface For Blood Cancer Detection,” *Langmuir*, vol. 29, no. 27, pp. 8753–8762, 2013.
- [22] U. Menczgar, J. Brunner, F. E., M. Gail, G. Abstreiter, H. Kibbel, H. Presting, and E. Kasper, “Photoluminescence Studies Of Si/Si_{1-x}Ge_x Quantum Wells And Simgen Superlattices,” *Thin Solid Films*, pp. 222–227, 1992.
- [23] T. P. Pearsall, J. Bevk, L. C. Feldman, J. M. Bonar, J. P. Mannaerts, and A. Ourmazd, *Phys. Rev. Lett.*, vol. 58, no. 729, 1987.

- [24] C. W. Liu, T.-H. Cheng, Y.-Y. Chen, S. R. Jan, C. Y. Chen, S. T. Chan, Y. H. Nien, Y. Yamamoto, and B. Tillack, *Thin Solid Films*, vol. 520, no. 8, pp. 3249–3254, 2012.
- [25] J. Liu, X. Sun, R. Camacho-Aguilera, L. C. Kimerling, and J. Michel, *Opt. Lett.*, vol. 35, no. 679, 2010.
- [26] T. M. Bruton, G. Luthardt, K. D. Rasch, K. Roy, I. A. Dorrity, B. Garrard, L. Teale, J. Alonso, U. Ugalde, K. Declerq, J. Nigs, J. Szlufcik, A. Rauber, W. Wettling, and A. Vallera, “A Study Of The Manufacture At 500 Mwp P.A. Of Crystalline Silicon Photovoltaic Modules,” in *14th European Photovoltaic Solar Energy Conference*, pp. 11–16.
- [27] M. A. Green, “The Future Of Crystalline Silicon Solar Cells” *Prog. Photovoltaics*, vol. 9, 2001.
- [28] M. A. Green, “Third generation photovoltaics: Ultra-high conversion efficiency at low cost,” *Prog. Photovoltaics Res. Appl.*, vol. 9, no. 2, pp. 123–135, 2001.
- [29] G. CONIBEER, “Third-generation photovoltaics,” *Mater. Today*, vol. 10, no. 11, pp. 42–50, Nov. 2007.
- [30] W. Shockley and H. J. Queisser, *J. Appl. Phys.*, vol. 510, no. 31, 1962.
- [31] M. A. Green, “Third Generation Photovoltaics: Solar Cells For 2020 And Beyond,” *Phys. E Low-dimensional Syst. Nanostructures*, vol. 14, no. 1–2, pp. 65–70, Apr. 2002.
- [32] A. Marti and G. L. Araujo, *Sol. Energy Mater. Sol. Cells*, vol. 43, no. 202, 1996.
- [33] A. S. Brown and M. A. Green, *Prog. Photovoltaics*, vol. 10, p. 299, 2002.
- [34] “Solar Junction Breaks Concentrated Solar World Record with 43.5% Efficiency.” [Online]. Available: Cnet.com (Last accessed on 5.09.2013).
- [35] R. R. King, “Band-Gap-Engineered Architectures for High-Efficiency Multijunction Concentrator Solar Cells,” in *21st Euro PVSEC*, 2006, p. 124.
- [36] J. Meier, *Thin Solid Films*, vol. 451, no. 518, 2004.
- [37] J. Yang, Proc. in *26th IEEE PVSC*, 1997, p. 563.
- [38] A. G. Aberle, *J. Cryst. Growth*, vol. 287, no. 386, 2006.

- [39] P. A. Basore, "Pilot Production Of Thin-Film Crystalline Silicon On Glass Modules," in *4th World Conf., PV Energy Conversion*, 2006, p. 2089.
- [40] G. Conibeer, M. Green, R. Corkish, Y. Cho, E.-C. Cho, C.-W. Jiang, T. Fangsuwannarak, E. Pink, Y. Huang, T. Puzzer, T. Trupke, B. Richards, A. Shalav, and K. Lin, "Silicon Nanostructures For Third Generation Photovoltaic Solar Cells," *Thin Solid Films*, vol. 511–512, pp. 654–662, Jul. 2006.
- [41] G. Conibeer, *Thin Solid Films*, vol. 511–512, 6, no. 654, 2005.
- [42] J. L. Vossen and W. Kern., *Thin film processes*. Academic Press, 1978.
- [43] D. A. Long, *Raman Spectroscopy*. McGraw-Hill, New York, 1977.
- [44] D. D. Sarma, P. K. Santra, S. Mukherjee, and A. Nag, "X-ray photoelectron spectroscopy: A unique tool to determine the internal heterostructure of nanoparticles," *Chemistry of Materials*, vol. 25, no. 8. pp. 1222–1232, 2013.
- [45] D. Schroder, *Semiconductor material and device characterization*. 2006.
- [46] S. L. Flegler, J. W. Heckman, and K. L. Klomparen, *An introduction Scanning and Transmission Electron Microscopy*. Oxford University Press, Inc., 1993.
- [47] H. Buebert and H. Janett, Eds., *Surface and Interface analysis*. Wiley-VCH Verlag GmbH, 2002.
- [48] C. D. Wagner, W. M. Riggs, L. E. Davis, and J. F. Moulder, *Handbook of X-RAY PHOTOELECTRON SPECTROSCOPY*. Perkin-Elmer Corporation, 1979, pp. 12–16.
- [49] H. Munder, *In Porous Silicon Science and Technology*. Les Editions de Physique, Les Ulis, 1995.
- [50] Skoog, *Principles of Instrumental Analysis (6th ed.)*. Belmont: Thomson Brooks/Cole, 2007, pp. 169–173.
- [51] E. Sabin, "High Temperature IDDQ Testing for Detection of Sodium and Potassium," *IEEE Int. Reliab. Phys. Symp.*, vol. 34, pp. 355–359, 1996.
- [52] J. Tauc, R. Grigorovici, and A. Vancu, "Optical Properties and Electronic Structure of Amorphous Germanium," *Phys. status solidi*, vol. 15, no. 2, pp. 627–637, 1966.

- [53] J. I. Pankove and D. A. Kiewit, "Optical Processes in Semiconductors," *Journal of The Electrochemical Society*, vol. 119, no. 5. p. 156C, 1972.
- [54] S. Knief and W. von Niessen, "Disorder, Defects, And Optical Absorption In a-Si and a-Si:H," *Physical Review B*, vol. 59, no. 20. pp. 12940–12946, 1999.
- [55] Y. Sasaki and C. Horie, *Phys. Rev. B*, vol. 47, no. 3811, p. 8, 1993.
- [56] C. WK, H. YW, N. SP, and N. V, *J Appl Phys*, vol. 89, no. 2168, 2001.
- [57] P. Tognini, L. Andreani, M. Geddo, A. Stella, P. Cheyssac, and R. Kofman, "No Title," *Phys Rev B*, vol. 53(11), no. 6992, 1996.
- [58] M. Vasilevskiy, A. Rolo, and M. Gomes, *Solid State Commun*, vol. 104, no. 381, 1997.
- [59] U. Serincan, G. Kartopu, A. Guennes, T. G. Finstad, R. Turan, Y. Ekinci, and S. C. Bayliss, "Characterization Of Ge Nanocrystals Embedded In SiO₂ By Raman Spectroscopy," *Semicond. Sci. Technol.*, vol. 19, no. 2, pp. 247–251, 2004.
- [60] N. Srinivasa Rao, A. P. Pathak, G. Devaraju, and V. Saikiran, "Growth And Characterization Of Nc-Ge Prepared By Microwave Annealing," *Vacuum*, vol. 85, no. 10, pp. 927–931, 2011.